A Study on the Influence of the Tube Layout on Sub-channel Hydrodynamics in a Bubble Column with Internals

Möller, F.; Lau, Y. M.; Seiler, T.; Hampel, U.; Schubert, M.;

Originally published:

January 2018

Chemical Engineering Science 179(2018), 265-283

DOI: https://doi.org/10.1016/j.ces.2018.01.008

Perma-Link to Publication Repository of HZDR:

https://www.hzdr.de/publications/Publ-26552

A Study on the Influence of the Tube Layout on Sub-channel Hydrodynamics in a Bubble Column with Internals

F. Möller[1,*], Y. M. Lau[1], T. Seiler[1], U. Hampel[1,2], M. Schubert[1]

[1]Insitute of Fluid Dynamics, Helmholtz-Zentrum Dresden-Rossendorf, Bautzner Landstr. 400, 01328 Dresden, Germany

[2]AREVA Endowed Chair of Imaging Techniques in Energy and Process Engineering, Technische Universität Dresden, 01062 Dresden, Germany

[*]Corresponding author

Keywords

Bubble column, heat exchanger internals, sub-channel analysis, local hydrodynamics, ultrafast X-ray tomography.

Abstract

In this work, the hydrodynamics of a bubble column with vertical heat exchanger internals in a narrow bubble column of D_i = 0.1 m inner diameter with a clear liquid height of L_c = 1.1 m was comprehensively studied. We applied ultrafast X-ray tomography to obtain hydrodynamic parameters, such as, gas holdup, bubble size distribution, bubble number flux and flow patterns at hitherto inaccessible positions within the sub-channels of the tube bundles. To investigate the influence of the tube bundle patterns, square and triangular pitches were considered. Tubes of d_o = 8 and 13 mm outer diameter were installed to study the effect of tube size, while maintaining approx. A_c = 25 % coverage of the cross-sectional area, which is typical for e.g. Fischer-Tropsch process operated in bubble column reactors. The superficial gas velocity was varied from u_g = 2 to 20 cm s^{-1} to cover homogeneous and heterogeneous flow regimes.

Internals' type and tube diameter were found to crucially influence the gas holdup distribution across the column diameter, which is known to generate liquid circulation, to shape the gas velocity profile and to cause intensive bubble interactions. The higher flow resistance induced by triangular tube configurations and dense tube patterns, which is attributed to the smaller hydraulic diameter of the respective configurations, forces bubbles to preferably rise near the column wall. Within the tube bundle, the radial holdup profiles show a pronounced non-parabolic trend, indicating zones of reverse liquid flow directions between the internal tubes. Furthermore, the gas-liquid flow morphology within various sub-channels was analyzed revealing a slug-like flow formation at superficial gas velocities larger than 10 $cm\,s^{-1}$.

1 Introduction

Bubble column reactors (BCRs) are widely applied apparatuses in the chemical and process industry used e.g. for hydrogenation, oxidation, waste water treatment etc., as they are simple in design, operate without moving parts and require comparatively low maintenance costs. Compared to typical tubular fixed bed reactors or continuous stirred tank reactors, BCRs offer advantageous heat and mass transfer characteristics at lower energy input (Deckwer et al., 1974; Shah et al., 1982). In particular, BCRs are preferred for highly exothermic reactions (Deckwer, 1992), such as Fischer-Tropsch synthesis (T ~ 400 °C, P ~ 200 bar, H_R = -210 $kJ\,mol^{-1}$) and methanol synthesis (T ~ 270 °C, P ~ 100 bar, H_R = -91 $kJ\,mol^{-1}$) (Casanave et al., 1999; Hawthorne et al., 2006; Hensman, 2004; Hugues et al., 2010; Kölbel and Ackermann, 1958; Lee et al., 2009; Maretto and Piccolo, 1998; Maretto et al., 2002). For safe and stable reactor operation with long catalyst lifetime and high product selectivity, heat exchangers are installed to ensure isothermal operation (Jasim, 2016; Schlüter et al., 1995; Sie and Krishna, 1999; Westermeyer-Benz, 1992). Mainly, vertical tube bundle internals are used to remove the reaction heat directly (Kölbel and Ackermann, 1958; Maretto and Piccolo, 1998) and to generate high pressure steam (Youssef, 2010) without additional expenses for large circulation pumps needed for external heat

exchangers. The produced heat of reaction defines the required volume-specific heat transfer area, which, in turn, determines the ratio of the reactor's cross-sectional area (CSA) occupied by the tube bundle. Typically, the CSA coverage is between 20 and 30% but can also reach up to 60% (Hugues et al., 2010; Maretto and Piccolo, 1998; Piccolo et al., 2012; Schlüter et al., 1995). It is known, that the hydrodynamics significantly depend on CSA coverage but due to the difficulties to perform experimental and numerical studies in such configurations, the public hydrodynamic data basis is scarce.

Some studies on the influence of the CSA coverage on gas holdup were conducted for BCRs with vertical heat exchanger tube bundles (Berg and Schlüter, 1995; Berg, 1993; Berg et al., 1994, 1992; Bernemann, 1989; Bernemann et al., 1991; Chen et al., 1999; De et al., 1999; Hamed, 2012; Pradhan et al., 1993; Westermeyer-Benz, 1992; Youssef and Al-Dahhan, 2009; Youssef, 2010), which confirmed in unison that the gas holdup increases with increasing coverage. At CSA coverage of 5% and below, however, the effect on the hydrodynamics was found negligible (Chen et al., 1999; Youssef and Al-Dahhan, 2009; Youssef, 2010). The most important results of the previous studies are summarized in Table 1 together with experimental designs and operating conditions.

Table 1: Summary of previous studies on bubble columns with internals and main results.

Authors	Column diameter [mm]	Tube configurations	Velocities [cm s^{-1}]	Measurement technique	Effect of internals
(Chen et al., 1999)	440	16 tubes (d_o = 25.6 mm, concentric arrangement in two rings)	u_g = 2 – 10	Radioactive particle tracking	▪ Slightly higher gas holdup ▪ No effect on gas-liquid recirculation pattern ▪ Lower turbulence levels due to the reduced length-scale of turbulence
(Larachi et al., 2006)	190 and 1000	Tube bundles (d_o = 25.6 mm) in four arrangements with 31 to 132 tubes	u_g = 12	CFD Simulations	▪ Lower turbulence level ▪ Core-annulus flow structure for evenly distributed internals
(Guan et al., 2014)	-	8 single sub-channels: tube configuration in square and triangular pitch (d_o = 12.7 and 25.4 mm with d_{ydh} ranging from 49.2 – 238.1 mm)	-	CFD simulations	▪ Coverage and pitch type have influence on the bubble rocking intensity and frequency ▪ Elongated bubbles are found ▪ Aspect ratio increases ▪ Bubble rise velocity decreases
(Bernemann, 1989; Bernemann et al., 1991)	90 and 450	10 tube bundle configurations (d_o = 25 mm), number of tubes varied between 5 and 63	u_g = 3 – 80 u_l = 0.5, 4.6	Flywheel anemometer, conductivity probes, pressure taps	▪ Local liquid velocity increases due to funneling effect ▪ Axial liquid velocity increases with increasing tubes number ▪ 1D axial dispersion model sufficiently depicts mixing ▪ Increased central liquid velocity leads to stronger large scale mixing
(Westermeyer-Benz, 1992)	120, 190, 190.6, 450	36 different configurations (d_o= 25 and 63	u_g = 1 – 60 u_l = 0 -4	Conductivity probes, pressure taps	▪ Heat transfer decreases with decreasing pitch size ▪ Heat transfer coefficient increases with increasing reactor diameters

		mm), number of tubes varied between4 to 97			
(Youssef and Al-Dahhan, 2009; Youssef, 2010; Youssef et al., 2014)	190 and 450	16 and 75 tubes (d_o= 2.56 mm)	u_g = 5 – 55 u_l= 0.5 – 1 (for liquid dispersion only)	Four point optical probe and visual observations	▪ Higher tube coverage leads to higher gas holdup ▪ Bubble chord length decreases ▪ Interfacial area increases ▪ Bubbles move rather downwards in the wall region ▪ Liquid mixing increases
(Hamed, 2012)	190 and 450	12 tubes (d_o = 2.56 mm) 48 tubes (d_o = 1.28)	u_g = 20 – 45	Four point optical probe, visual observations, helium gas analyzer	▪ Centerline gas velocity increases ▪ Turbulent intensity decreases ▪ Gas phase mixing decreases ▪ No effect on mass transfer as local turbulence decreases and interfacial area increases simultaneously
(Jhawar and Prakash, 2014; Jhawar, 2011)	150	15 tubes (d_o= 12.7 mm) Concentric baffle	u_g = 3 -35	Pressure taps, heat transfer probe/ thermocouple	▪ Overall heat transfer increases ▪ Bubble size decreases ▪ Steeper heat transfer coefficient profiles ▪ Gas holdup increases ▪ Liquid velocity decreases
(George, 2015)	150	15 tubes d_o =9.5 mm)	u_g = 1 – 30	Pressure taps, phytography,	▪ Complex flow structures are encountered ▪ Gas holdup increases ▪ Interfacial area increases ▪ Liquid mixing increases which leads to a decreasing mixing time
(Forret et al., 2003)	1000	56 tubes (d_o= 63 mm)	u_g = 15	Conductivity probes	▪ 2D dispersion models are needed to describe the mixing ▪ Large scale recirculation is enhanced due to higher centerline liquid velocity
(Jasim, 2016)	140	30 tubes (d_o= 12.8 mm) 8 tube s(d_o= 25.6 mm)	u_g = 2 – 45	Four point optical probe	▪ Asymmetrical flow when hexagonal internal are inserted ▪ Bubble chord length decreases leading to slower bubble rise velocities ▪ Smaller internals: core holdup increases ▪ Larger internals: bubble chord length increases which

					leads to a higher bubble velocity

The increase in gas holdup is basically attributed to the smaller bubbles rising at lower velocity as a result of the intensified bubble breakup, which is the prevailing mechanism in BCRs with dense vertical internals (Berg, 1993; Bernemann, 1989; Bernemann et al., 1991; Jhawar and Prakash, 2014; Korte, 1987; Youssef and Al-Dahhan, 2009; Youssef, 2010; Youssef et al., 2013). This enhanced breakup rate is caused by smaller eddies confined by the tube walls (Westermeyer-Benz, 1992), which increase eddy wavenumber and eddy concentration (Prince and Blanch, 1990). The increased number of bubbles as a result of inserted internals was experimentally proven via four-point optical probes (Jasim, 2016; Kagumba and Al-Dahhan, 2015; Kagumba, 2013; Youssef and Al-Dahhan, 2009; Youssef, 2010) in terms of higher bubble number flux. However, these bubble size measurements are limited to the bubble chord lengths only, which are obtained by local probes. In addition, those sizes depend strongly on the radial position of the tubes and an overall estimation of the cross-sectional bubble size distribution is not possible. Furthermore, reduced bubble chord lengths obtained for higher occupation of the CSA at selected radial positions confirmed the occurrence of smaller bubbles due to enhanced breakup, too (Hamed, 2012; Jasim, 2016; Kagumba, 2013; Youssef, 2010). The use of helical coils was found to further amplify the breakup and, thus, to increase the gas holdup (De et al., 1999).

The wall surface structure of inserted tubes revealed additional effects. Guan et al. (2015) installed pin-finned internals with a CSA coverage of up to 10%, which shaped a strong non-parabolic radial holdup profile already at such low coverage. Contrary to plain tube internals, the fins further hinder a straight upward rising path of the bubbles in the sub-channels and induce pronounced lateral movement. A schematic depiction of a typical holdup profile for bubble columns with internals is shown in Figure 1.

Liquid velocity measurements obtained via fly wheel anemometer and Computer-Automated Radioactive Particle Tracking, respectively, by Bernemann (1989), Bernemann et al. (1991) and Chen et al. (1999), revealed that the liquid velocity profile in bubble columns shows stronger peaking if internals are inserted, leading to an enhanced liquid circulation. The inversion point,

however, remains at the same position. However, it is to be noted that Bernemann (1989) used the same volumetric flow rate instead of the effective superficial gas velocity for the measurements, which leads to misinterpretation as the superficial gas velocity is higher compared to the empty BCR counterpart. Contrary to rather straight rising bubbles in empty columns, Youssef (2010), Hamed (2012) and Jasim (2016) observed that a considerable ratio of the bubbles moves along a descending trajectory if internals are inserted. This is an indication for large liquid circulation cells similar to airlift reactors (Berg, 1993; George, 2015; Jhawar and Prakash, 2014), while smaller circulation cells of only half column diameter size are stacked above each other in empty BCRs (Zehner, 1988). Such liquid circulation motion was also confirmed by Forret et al. (2003) via conductivity tracer measurements in a large diameter bubble column equipped with internals. Only the extension of the axial dispersion model considering liquid circulation velocity as well as radial dispersion enabled describing the spatiotemporal tracer spreading.

In contrast to the experimental findings, for example, by Bernemann (1989) and Bernemann et al. (1991), computational fluid dynamics (CFD) simulations by Larachi et al. (2006) and Laborde-Boutet et al. (2010) using an Eulerian-Eulerian two-phase model showed that internals alter the parabolic liquid velocity profile for lab-scale and industrial bubble column reactors, as every tube enforces an additional no-slip boundary condition reducing the radial momentum transport and this way equalizing the holdup profile. The predicted parabolic shape for the radial gas holdup profile in empty bubble columns converted into a shape with the maximum gas holdup in the vicinity of the internals, which is explained by the existence of bubble trains and swirling motion preferably close to the column wall. Furthermore, Larachi et al. (2006) found that the liquid kinetic turbulent energy is noticeable smaller compared to empty BCRs, since the largest turbulent eddies depend on the tube pitch of the internals. Eventually, it should be noted that previously reported profiles were based on experimental data from very few accessible radial positions throughout the bubble column's diameter only, and the local holdup values in the immediate vicinity of the inserted tubes was hitherto fully ignored due to the low spatial

resolution of the measurement techniques used. Considering the no-slip boundary condition at the tube walls and the low gas holdup in the immediate vicinity as shown by Larachi et al. (2006) and Laborde-Boutet et al. (2010), the assumed liquid velocity profile in columns with internals is schematically depicted in Figure 1.

Regarding the heat transfer, Jhawar and Prakash (2014) have shown that the heat transfer coefficient is increased when adding a ring like tube bundle into the reactor. Furthermore, they have shown that the centerline liquid velocity is increasing when inserting such structures.

Hitherto, only very few studies addressed the particular effects of tube configuration and tube diameter on the hydrodynamic characteristics. Yamashita (1987) revealed no difference in gas holdup and heat transfers coefficient for various tube configurations in terms of bundle patterns, as long as the tubes are evenly distributed. Contrary, Jasim (2016) showed that circularly arranged internals promote flow symmetry, while internals with triangular pitch induce asymmetric flows, which was also confirmed by other research groups (Al-Mesfer et al., 2016; Guan et al., 2015, 2014; Larachi et al., 2006). Although similar results were provided by Kagumba (2013) and Kagumba and Al-Dahhan (2015), it is not fully clear whether the flow was mainly altered by the tube size or the pattern since both were modified at once in the respective configurations. From the available literature, it is also not clear if the bottom end of the internals (i.e. U-tube bottom design heat exchanger or flat end of the bundle) and the distance to the sparger are of any concern.

While the global column hydrodynamics with inserted internals were analyzed as summarized above, the sub-channel two-phase flow structures have not been addressed experimentally. Only one CFD study using VOF for sub-channels arranged in square and triangular pitch, respectively, with two different tube diameters was performed (Guan et al., 2014). The hydraulic diameter of the sub-channel was identified as the most significant parameter for bubble shape, size and trajectory. Thus, the tube diameter was suggested as the most appropriate scaling dimension, while keeping the hydraulic diameter constant. However, such scale-up strategy hardly holds for

heat transfer, since the specific surface area is the most important design parameter, which does not necessarily correlate with the hydraulic diameter. Furthermore, it should be mentioned that this study ignored any exchange between neighboring sub-channels, which is expected to significantly influence bubble trajectories and liquid mixing.

Figure 1 congregates schematically the authors' perception of the effects of internals on radial holdup, radial liquid velocity, eddy size, liquid circulation and mixing pattern drawn from the literature in comparison with an empty column. The higher flow resistance induced by the bundle and the no-slip boundary condition at the tube walls alter the parabolic nature of holdup and liquid velocity profiles, which are strongly linked with each other (Gupta et al., 2001; Schweitzer et al., 2001; Vitankar and Joshi, 2002). Within the individual sub-channels, pronounced liquid velocity gradients are expected. The liquid mixing in BCRs with inserted tube bundles is a result of small-scale circulation cells superimposed by a large liquid circulation (Forret et al., 2003), which, in turn, leads to slower radial liquid spreading. As found by other researchers (Bernemann, 1989; Bernemann et al., 1991), the insertion of tube bundles leads to a funneling effect of the liquid, which causes the slow radial spreading. This, in turn, leads to the overlapping of the large-scale liquid circulation - similar to an air-lift reactor (Berg, 1993; George, 2015) - with small sub-channel-scale circulations due to the additional walls. Furthermore, the zoom view on the right hand side depicts the circulation cell model (with cells stacked above each other) proposed by Joshi and Shah (1981) scaled down to the sub-channel.

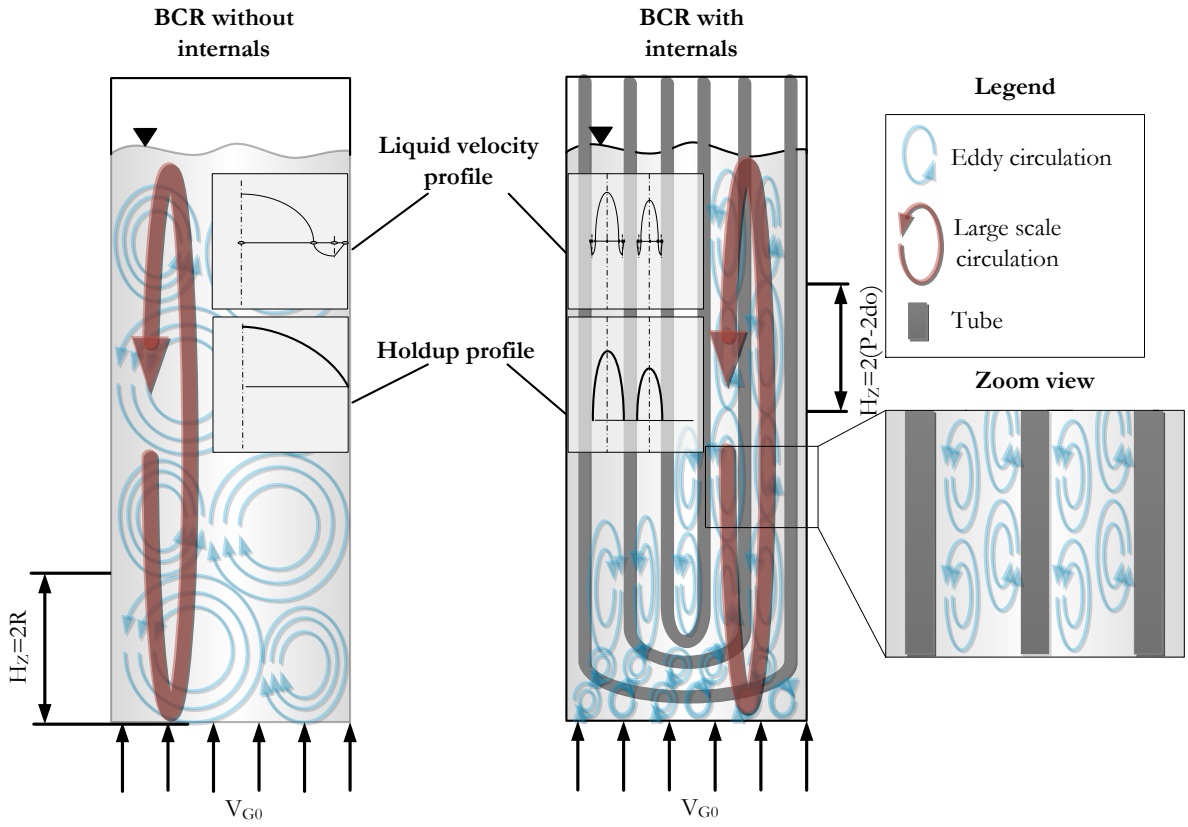

Figure 1: Schematic illustration of characteristic hydrodynamic and mixing patterns of bubble columns without (left) and with (right) internals.

The main objective of this study is to characterize the sub-channel hydrodynamics in a bubble column equipped with vertical internals maintaining a coverage of approx. 25 % of the CSA for square and triangular pitch configurations. Such configurations are proposed by the Tubular Exchanger Manufacturers Association (TEMA) design for shell and tube heat exchangers (Shah and Sekulic, 2003; Thulukkanam, 2013). In particular, the influence of the tube diameter is addressed (8 and 13 mm). Industrial vertical heat exchanger tube bundles typically have a U-shaped bottom design (Thulukkanam, 2013). Therefore, this study addresses the influence of tube pattern as well as tube size on the hydrodynamics, while maintaining the same cross-sectional coverage. Being interested mainly in the sub-channel flow in different cross-sectional tube arrangements, we used a simplified tube bundle design with straight tubes being cut and

sealed at the bottom, but compared the results with an exemplary U-tube bottom design, especially to clarify the effect of this design on initial gas distribution.

The whole study is based on an advanced analysis utilizing the non-invasive ultrafast X-ray computed tomography to disclose flow pattern, bubble size distribution, bubble number flux and holdup profiles even in the sub-channels. While previous studies were limited to few radial measurement positions only, this measurement technique enables detailed insights into the sub-channels with a spatial resolution down to 0.5 mm in order reveal interactions between bubbles and internals even close to the vicinity of the tubes. This will support the analysis of the patterns altered by internals.

2 Experimental design and measurement methods

In this chapter the experimental setup is described including the design of the various inserted vertical tube bundles. Furthermore, the applied imaging technique and the corresponding post-processing routines for the data extraction are shown.

2.1 Bubble column setup and operating conditions

The experiments were performed on a cylindrical bubble column with an inner diameter of $D_\mathrm{i} = 0.1\,\mathrm{m}$ and a total length of $L = 2\,\mathrm{m}$ (Figure 2a). The gas flow comes through a perforated plate with $n = 55$ holes of $d = 0.5\,\mathrm{mm}$ diameter arranged in a triangular pitch ($P = 0.01\,\mathrm{m}$) resulting in an open area ratio of $A_\mathrm{o} = 1.4\,\%$. Superficial gas velocities ranging from $u_g = 2$ to $14\,\mathrm{cm\,s^{-1}}$ with increments of $2\,\mathrm{cm\,s^{-1}}$ were precisely adjusted via two mass flow controllers (Omega, FMA-2608A and FMA-2611A) to cover homogeneous and heterogeneous flow regimes. In addition, an experiment at $u_\mathrm{g} = 20\,\mathrm{cm\,s^{-1}}$ was performed at well-developed churn-turbulent flow conditions. For the sake of comparability with the empty column counterpart, all superficial gas velocities are based on the area of the CSA not occupied by the

tube bundle. Deionized water and air were used for the experiments and the unaerated liquid height was kept constant at L_c = 1.1 m for all experiments.

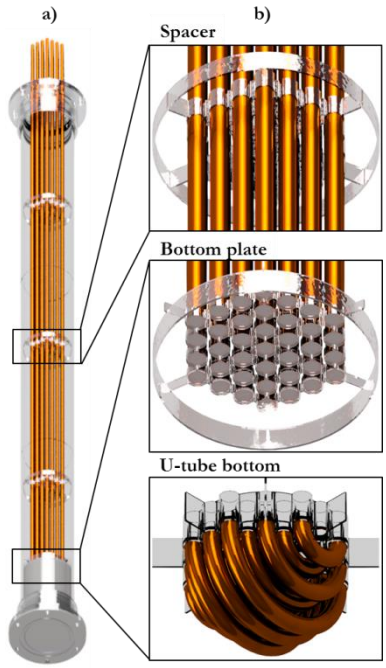

Figure 2: Experimental setup a) bubble column design b) spacer design, flat bottom bundle and U-tube bundle.

Table 2: Summary of the tube layouts and their specification as well as their geometrical data.

	Square 8 (*s8*)	**Triangular 8 (*t8*)**	**Square 13 (*s13*)**	**Triangular 13 (*t13*)**
Type	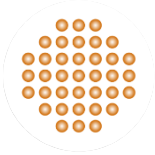	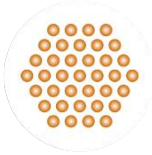	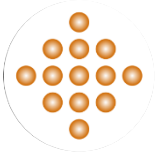	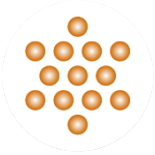
Diameter (d_o) in mm	8.0	8.0	13.0	13.0
Pitch (P) in mm	11.0	11.5	17.5	18.5
Hydraulic diameter (d_h) in mm	7.6	5.6	11.8	8.9
Sub-channel area (A_s) in mm^2	70.7	32.1	173.5	81.8

Coverage (A_c) in %	24	24	23	23
Number of tubes (N)	37	37	13	13

2.2 Design of internals

The pitches of the internals were chosen according to the TEMA (Thulukkanam, 2013) manufacturing instructions. For an effective heat transfer, the heat exchanger layout guidelines propose a pitch-to-tube diameter ratio of approx. 1.3. The number of tubes was chosen to ensure a large surface-to-volume ratio providing a heat removal capacity typical for the Fischer-Tropsch synthesis in BCRs. The area covered by the internals was adjusted at approx. 25 % regardless of tube size and tube pattern. Tubes of 8 mm and 13 mm outer diameter, respectively, were selected and arranged in square and triangular pitch (Table 2). The geometrical details of the internals are summarized in Table 2. It should be noted that the wall zone (dimensionless radius $r/R \geq 0.75$) was kept free of internals to ensure better heat removal and easier maintenance as suggested by Li and Prakash (2001) and Youssef (2010). Since a rather narrow bubble column was used, the geometrical details were scaled down from larger columns. As scaling quantitates, coverage, pitch-to-tube diameter and ratio of the free wall region were used. The tube bundles were tightly fixed with several 3D printed spacer grids installed at axial distances of 50 cm. The distance between the bottom tube ends and the sparger plate was same as the clearance between wall and bundle. To mimic industrial heat exchangers, a U-tube bottom design was also studied (see Figure 2b).

2.3 Ultrafast X-ray computed tomography

The ultrafast electron beam X-ray computed tomography (CT) (Figure 3) was used to visualize non-invasively the gas-liquid flow structure within the sub-channels confined by the tubes at very high temporal resolution (Fischer et al., 2008). Contrary to conventional medical X-ray CT systems, an electron beam is rapidly swept along a tungsten target surrounding the column to

create the moving X-ray spot. 432 detector elements arranged on a circular detector ring measure the arriving intensities of X-rays penetrating the bubble column. The measurements to capture the transient gas-liquid flow structure were performed at a frequency of 1000 cross-sectional images per second. More information on the principles of the ultrafast electron beam X-ray computed tomography and its technical details can be found elsewhere (Banowski et al., 2017; Bieberle and Barthel, 2016; Bieberle et al., 2012, 2011, 2007; Möller et al., 2017; Wagner et al., 2015).

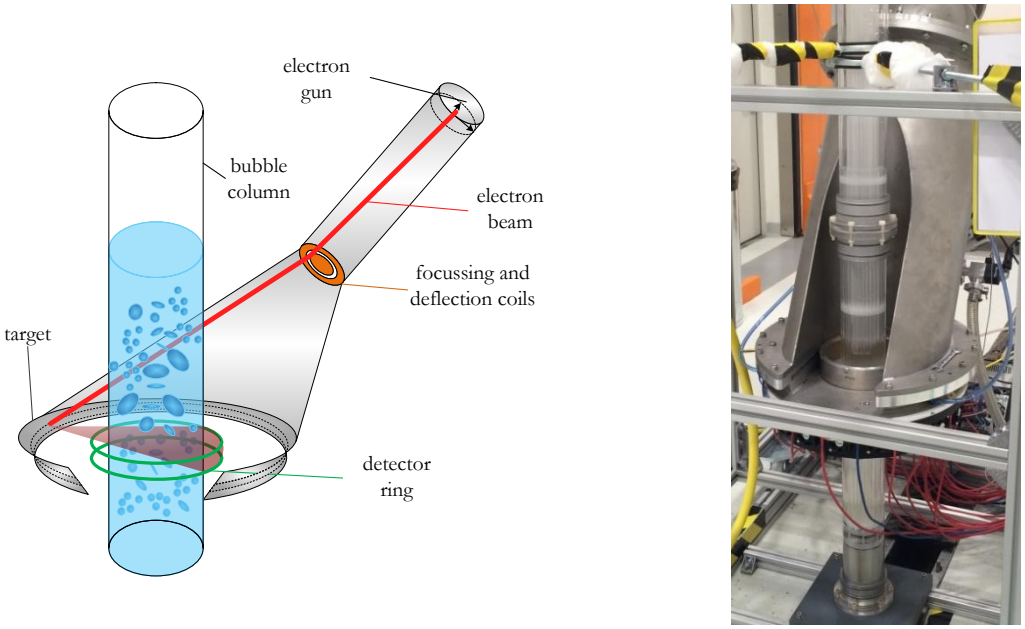

Figure 3: Functional principle (left) and lab view (right) of the ultrafast X-ray tomograph.

2.4 Tomography data post-processing

To obtain phase fraction (holdup) data at every particular position in the CSA, a step-wise post-processing procedure was applied as illustrated in Figure 4. At first, a reconstructed cross-sectional raw image is obtained via filtered back-projection of the data matrix comprising the detector readings from one beam revolution. Then, the image is normalized between empty and liquid-filled BCR returning pixel values of 0 and 1 for gas and liquid phase, respectively, while

values between 0 and 1 represent gas-liquid mixtures and the column wall returns values > 1. Subsequently, the referenced data $(\boldsymbol{\mu}_\mathrm{r})$ are obtained subtracting the empty bubble column reference data $(\boldsymbol{\mu}_\mathrm{e})$ from the normalized data $(\boldsymbol{\mu}_\mathrm{n})$ and from the liquid-filled bubble column reference data $(\boldsymbol{\mu}_\mathrm{f})$, respectively, and by dividing the differences according to

$$\boldsymbol{\mu}_\mathrm{r} = \frac{\boldsymbol{\mu}_\mathrm{n} - \boldsymbol{\mu}_\mathrm{e}}{\boldsymbol{\mu}_\mathrm{f} - \boldsymbol{\mu}_\mathrm{e}} \,. \tag{1}$$

Then, the images are binarized via global threshold (0.65) and all cross-sectional images are stored and stacked as a 3D data matrix. Eventually, algorithms for the extraction of characteristic hydrodynamic data, such as, gas holdup, bubble number flux, radial gas holdup and bubble size distribution (BSD) are applied.

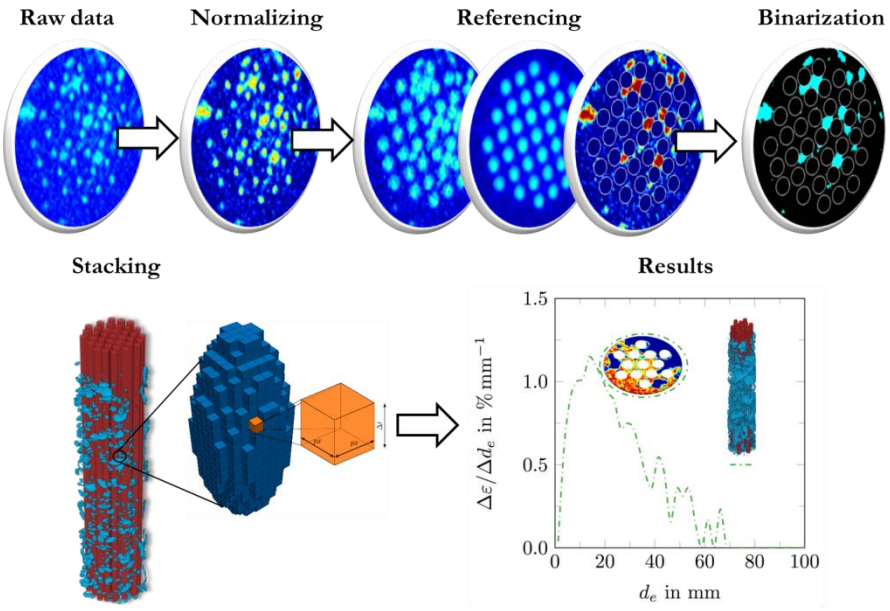

Figure 4: Flow chart of the data post-processing steps (data shown as pseudo color images for easier understanding).

For the calculation of the BSD, individual bubbles are identified from the 3D data matrix. In order to account for noise and artefacts, bubbles smaller than four pixels and those not detected in at least three consecutive frames were withdrawn from further analyses (Banowski et al., 2015). Each bubble is represented by a cluster of n voxels. The physical volume of a voxel is $\mathrm{l}_V^2 \cdot u_\mathrm{b} \cdot \Delta t$, with $l_V = 0.5\,mm$ being the voxel edge length, Δt the time between two subsequent images and u_b the bubble velocity. The latter can be determined in different ways, e.g. by cross-correlation (Barthel et al., 2015), bubble pairing (Banowski et al., 2017) or by taking the average swarm velocity according to (Deckwer, 1992) as $u_\mathrm{b} = u_\mathrm{g}/\varepsilon_\mathrm{g}$ with the given superficial gas velocity u_g and the cross-sectional gas holdup ε_g measured by the X-ray tomography. Having employed the latter method we calculated the individual bubble volumes as

$$V_\mathrm{b} = n_\mathrm{b} \cdot \mathrm{l}_V^2 \cdot u_\mathrm{b} \cdot \Delta t \quad , \tag{2}$$

Assuming an approximately spherical bubble shape, the hydraulic diameter can be calculated from the volume of an equivalent sphere as

$$d_\mathrm{e} = \left(\frac{6\,V_\mathrm{b}}{\pi}\right)^{\frac{1}{3}}. \tag{3}$$

Further details on the post-processing of the ultrafast X-ray tomography data for multiphase flows can be found by Banowski et al. (2015) and Lau et al. (2016).

2.5 Error analysis

As measurement repetitions are costly with regards to measurement time, data acquisition and post-processing, one measurement per superficial has velocity was carried out. Therefore, this section aims at estimating the possible error for the derived hydrodynamic data.

For post-processing purposes, a two-point calibration process was used to cope with image artifacts caused by beam hardening and scattering. As already mentioned by other authors (Azizi et al., 2017; Bieberle et al., 2012; Lau et al., 2016), the optimal threshold value to distinguish gas and liquid phase for bubble flows was determined as 0.65 based on static phantom measurement to ensure less than 10 % error for the estimated equivalent diameter. For a measurement frequency of 1000 frames per seconds, an ellipsoidal bubble of 10 mm diameter with an aspect ratio of 0.6 and a rise velocity of 21 $\mathrm{cm\,s^{-1}}$ is detected in 28 subsequent frames, which is sufficient to reach a measurement error of less than 5 %. A measurement duration of 6 s was identified sufficient for statistical averaging to obtain reliable data for the radial holdup profile as well as for the bubble size distribution. As a consequence, 10 s measurement durations were performed for all experiments to ensure time-independent results.

3 Results and discussion

In this chapter the results from the hydrodynamic study of the bubble columns with internals of various patterns are shown and compared with the empty bubble column counterpart.

Preliminary measurements taken at various dimensionless column heights revealed that the fully devolved flow region, i.e. equilibrium zone, is reached at z/D = 5.0, which confirms former findings (Wilkinson et al., 1992). Figure 5 indicates that no further change in BSD (upper row) and radial holdup (lower row) occurs from z/D = 5.0 to z/D = 7.0 in the homogeneous (u_g = 2 $\mathrm{cm\,s^{-1}}$) and heterogeneous flow regime (u_g = 10 $\mathrm{cm\,s^{-1}}$), respectively. Thus, only data from z/D = 5.0 are shown and discussed below.

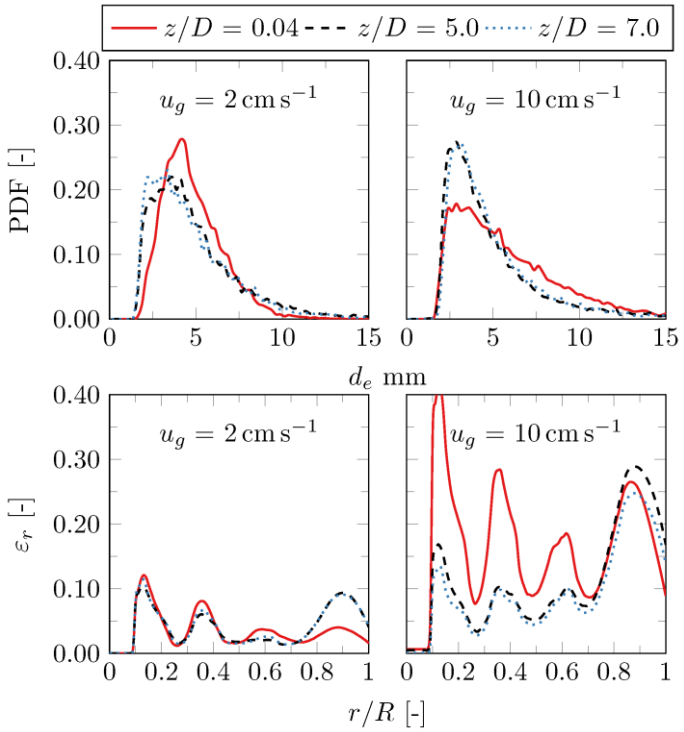

Figure 5: Bubble size distribution (upper row) and time-averaged radial holdup profile (lower row) for different distances from the gas sparger for the configuration square 8 (*s8*).

3.1 Gas holdup

Below, the results for gas holdup and bubble properties are discussed for the entire cross-section and for selected sub-channels representing internals' core and outer zone as well as the column wall region, respectively. The gas holdup distributions are utilized to draw conclusions regarding the liquid circulation patterns.

3.1.1 Cross-sectional gas holdup

The column total gas holdup is a crucial design parameter for bubble column reactors (Shah et al., 1982). In Figure 6, the cross-sectional holdup distributions are shown for all bundle configurations as well as for empty bubble (*e*) column and the U-tube bottom design (*su8*) for velocities ranging from homogeneous to heterogeneous flow regimes. The cross-sectional holdup data as well as the corresponding masks can be viewed in the supplementary material.

The holdup increases with increasing gas velocity for all configurations. The gas holdup in the empty BCR (*e*) forms the typical parabolic gas holdup profile at higher superficial gas velocities (Deckwer, 1992; Luo and Svendsen, 1991; Schweitzer et al., 2001). For the bubble column with internals, however, the profile changes and highest holdup values are found near the wall. Since the wall zone ($r/R \geq 0.75$) was kept free of internals, highest flow resistance is in the core of the column. Thus, bubbles preferentially rise in the wall zone, which was also reported by Larachi et al. (2006), for a configuration with a free wall area. Compared to the triangular configurations (*t8* and *t13*), more homogeneous gas holdup distribution is obtained for the square configurations (*s8* and *s13*). The comparably lower gas fraction in the core zone of the triangular configurations (compare Figure 6b and 6c as well as Figures 6d and 6e) can be attributed to the smaller sub-channels with approx. 25% smaller hydraulic diameters and, accordingly, to higher flow resistance in particular at high superficial gas velocities. A pronounced effect of the U-tube bottom design (*su8*) can be observed in the gas holdup distribution (compare Figure 6e and 6f). Increasing the gas velocity, results in a distinct phase maldistribution with clearly lower gas fraction within the bundle caused by the gas displacement effect of the bottom structure.

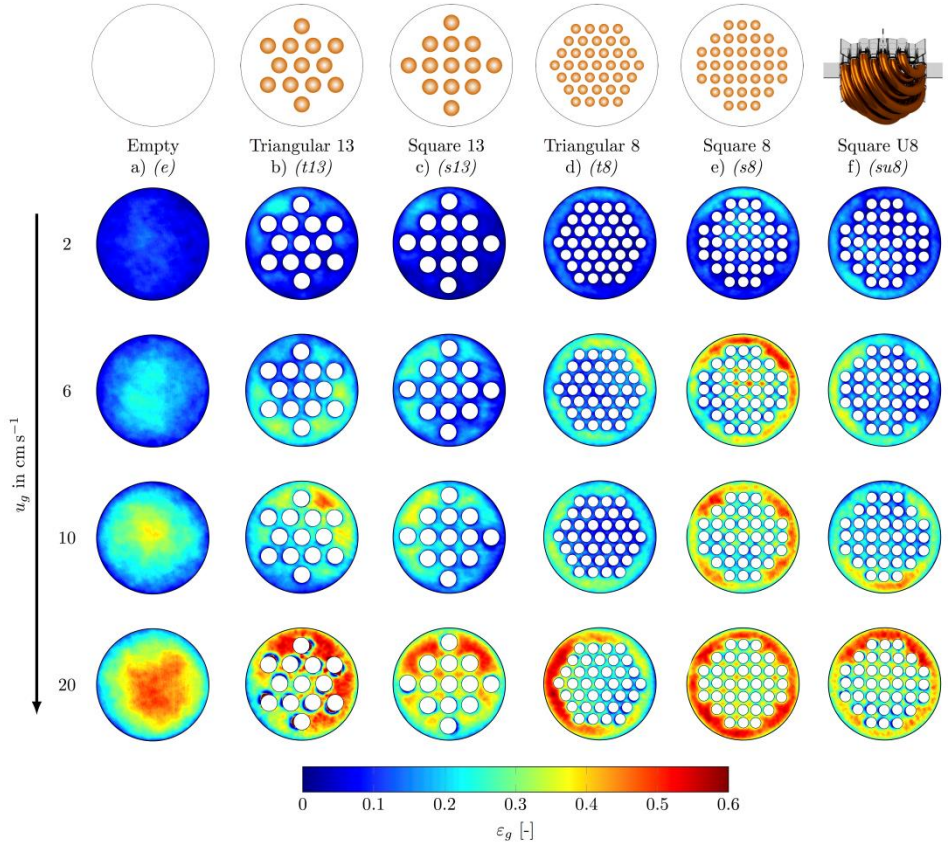

Figure 6: Time-averaged cross-sectional holdup distribution for a) *(e)*, b) *(t13)*, c) *(s13)*, d) *(t8)*, e) *(s8)* and f) *(su8)*.

The gas holdup profile correlates with the liquid velocity profile (Schweitzer et al., 2001; Wu et al., 2001) in such way that the liquid is propelled by the rising gas bubbles. Accordingly, zones of high gas holdup in the reactor's cross-sectional area denote zones of ascending liquid, while zones of low gas holdup account for descending liquid. Consequently, the cross-sectional gas holdup plots indirectly return the liquid velocity profile and allow concluding reasonably well on the liquid circulation patterns. In Figure 6, looking for example at the gas holdup distribution for the square 8 (*s8*) and square 13 (*s13*) configurations at $u_g = 20\,\mathrm{cm\,s^{-1}}$, the color code indicates lowest gas holdup between each neighboring tube along their shortest distance (tube bridges) and highest holdup at the wall area and within the sub-channel centers. It can be concluded that the inserted internals divide the liquid velocity field in ascending zones (sub-channels) and descending zones (tube bridges and near the wall). Accordingly, liquid circulation eddies form

within the sub-channels with characteristic dimensions of approx. half the sub-channel size or pitch of the tubes, respectively. This leads to a strong decrease in the liquid turbulent kinetic energy and its turbulent length scale, which is a measure of the energy level in the liquid phase caused by the larger turbulent structures (Jakobsen et al., 2005), having a strong impact on the circulation patterns (Laborde-Boutet et al., 2010; Larachi et al., 2006). From those plots one can concluded that large liquid cells circulate towards the tube bundle as already schematically depicted in Figure 1. Furthermore, asymmetric flow patterns are observed as also found by Al-Mesfer et al. (2016), Jasim (2016) and Kalaga et al. (2017). After starting the aeration of the bubble column with inserted internals, certain gas holdup pattern asymmetry evolves at steady-state conditions. The exact formation of asymmetry, however, is a random process and might differ after shutdown and restart of the column operation Thus, it can be clearly concluded that internals provoke asymmetric holdup pattern. Any effect of the least column inclination etc. can be fully excluded since particular care was taken to install a perfect upright column.

Figure 7 shows the average cross-sectional gas holdup vs. superficial gas velocity for all configurations and bottom structures referring to the respective free area of the cross-section (i.e. area occupied by the tubes is subtracted).

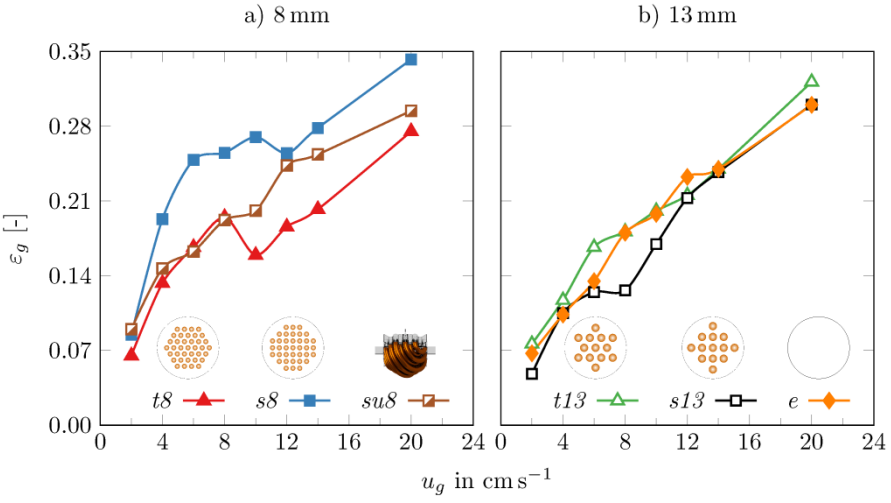

Figure 7: Gas holdup vs. superficial gas velocity for all configurations and bottom end structures.

The patterns of the internals have a strong influence on the holdup vs. superficial gas velocity's shape and magnitude caused by the bubble-tube interactions within the tube bundle. Regardless of the superficial gas velocity, the highest holdup was measured for the square 8 (*s8*) configuration (Figure 7a), whereas the lowest holdup was determined for the configurations triangular 8 (*t8*) and square 13 (*s13*) (Figure 7a and 7b). The gas holdup of the empty (*e*) bubble column counterpart is in between the 8 and 13 mm configurations. The lower holdup for the triangular 8 configuration can be attributed to the larger flow resistance induced by the internal layout, which forces the bubbles to rise outside the bundle. Here, the wall stabilizes the bubbles, which leads to the generation of larger bubbles and, hence, lower holdup. In case of 13 mm tubes (*t13* and *s13*) with larger hydraulic diameters, larger bubbles are created and stabilized by the tube walls forming one sub-channel. However, the differences between 13 mm tubes and the empty bubble column are almost negligible. Furthermore, the smaller sub-channels for the triangular 8 (*t8*) configuration forces bubbles to preferentially rise outside the tube bundle. Hence, larger bubbles, which are being stabilized by the column wall in the triangular 8 (*t8*) configuration, move somewhat faster compared to the square 8 (*s8*) configuration, where more bubbles are trapped in the sub-channels leading to funneling effects. The additional friction in the square 8 (*s8*) sub-channel, leads to slower bubble rise velocities and, therefore, increases the holdup.

Findings from other research groups (Hamed, 2012; Jasim, 2016; M. Kagumba and Al-Dahhan, 2015; Kagumba, 2013) show similar holdup trends, although the difference between empty BCR and BCR with internals is rather more pronounced, which may be attributed to the differences in internals' layout and size of the free wall region.

For the configurations square 8 (*s8*), square 13 (*s13*) and triangular 8 (*t8*), an S-shaped curve is observed (peaking at 8 to 12 $cm\,s^{-1}$) for the gas holdup denoting the transition region from homogeneous to heterogeneous flow conditions as a consequence of the coalescence of small bubbles and the generation of random bubble clusters accompanied by local liquid circulations

(Urseanu, 2000). Such transitional trends are known to occur mainly for sintered plates with tiny orifices producing narrow BSDs (Drahoš et al., 1991). Although a comparably coarse sparger was used in this study, the dense tube patterns of the inserted internals force the bubble breakup and, thus, show similar trends. For the configurations with larger tubes, however, the steady increase, known from spargers with larger holes (Deckwer, 1992; Drahoš et al., 1991; Sharaf et al., 2016), is observed with the only exception being the square 13 (*s13*) configuration, which shows a slight plateau at 8 $cm\,s^{-1}$ indicating the onset of the formation of larger bubbles. A similar holdup trend compared to the larger tubes is also obtained for the U-tube bottom design (*su8*). However, the gas holdup is significantly lower compared to the flat bottom structure (*s8*) but still higher than for the triangular (*t8*) as well as the empty bubble column (*e*) counterparts, which was also confirmed by the holdup distribution plots in Figure 6 revealing a pronounced maldistribution for the U-tube bottom design (*su8*). Furthermore, the course of the holdup profile changed, which is attributed to the agglomeration of the bubbles underneath the bottom, forcing a spiral flow and thus, an earlier transition towards a heterogeneous bubbles size distribution.

It is known that the gas holdup increases when inserting internals due to larger bubble-bubble and bubble-internal interactions enhancing the breakup rates (Bernemann, 1989; Bernemann et al., 1991; Youssef and Al-Dahhan, 2009; Youssef, 2010). The measurement data in Figure 6 and 7, however, show a rather ambiguous effect of the internals' structure (pitch, tube size and diameter) on the column total gas holdup. For the square 8 (*s8*) configuration, the tubes fence the bubbles in the resulting sub-channels and obstruct an effective radial exchange with neighboring sub-channels. Within the sub-channels, the trapped bubbles interact with the surrounding tubes and rise at lower velocity leading to higher holdup. Contrary, for triangular configurations with 8 mm tubes (*t8*), the larger flow resistance induced by the bundle forces the bubbles to preferentially rise outside the bundle.

All in all, contrary to the results from Yamashita (1987), the results show that the hydrodynamics are affected by the tube pattern and size.

3.1.2 Sub-channel gas holdup structure

To further highlight the impact of the internal tube bundles, the time-averaged gas holdup profiles are shown in Figure 8 drawn from the gas holdup patterns in Figure 6. Prior to the circumferential averaging, the area occupied by the internal tubes was masked. To support interpretation of the data we added a plot of the radial free hydraulic area distribution at the bottom of Figure 8.

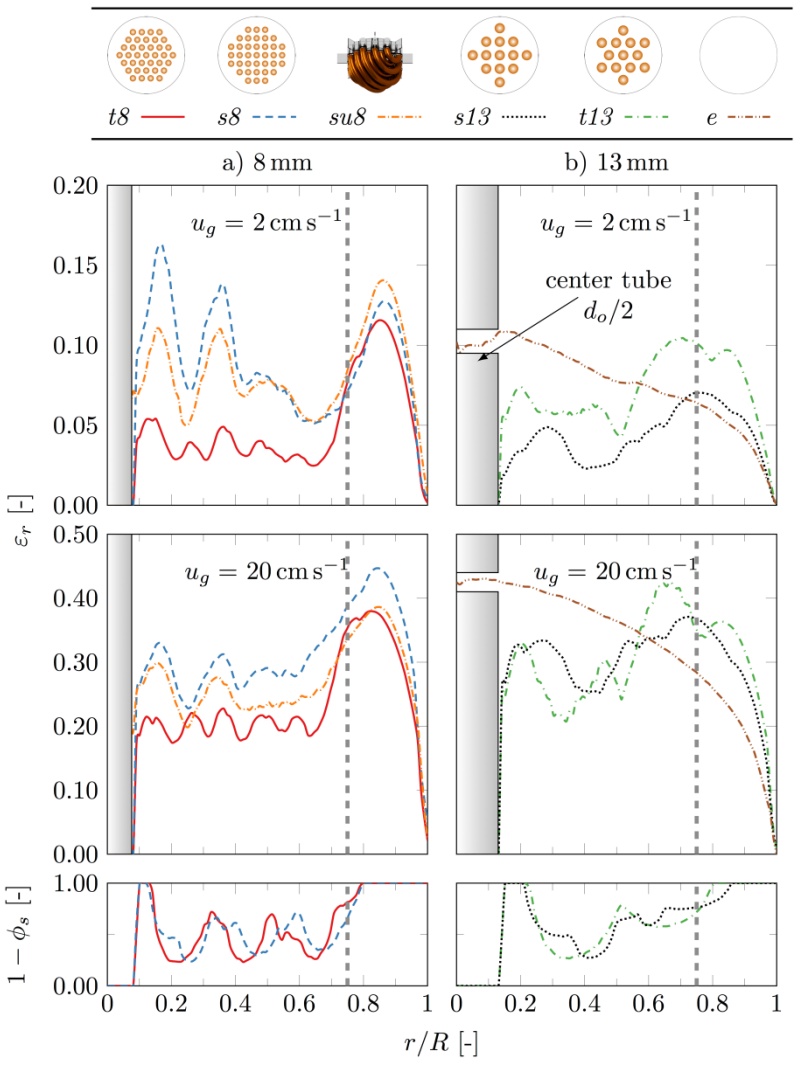

Figure 8: Time-averaged radial holdup profiles for selected superficial gas velocities corresponding to homogeneous (upper row) and heterogeneous (lower row) flow regime (grey bar indicate the sectional view of the center tube; dashed grey line denotes the zone occupied by the internals). The bottom row shows the radial profile of the free hydraulic area, that is, the fraction of cross sectional area outside the tubes relative to the total area averaged over small rings of equal radius.

For the empty BCR (Figure 8b), the typical parabolic profiles are obtained, which change significantly when inserting internals. The low gas holdup in the vicinity of the tubes (see Figure 6) is reflected by the oscillatory profile for $r/R < 0.75$, which coincides with the radial free space distribution of the tubes. For $r/R \geq 0.75$, the holdup profiles shape distinct peaks in the bundle-free wall region. It should be noted that such oscillatory curves were hardly reported in previous experimental studies (Hamed, 2012; Jasim, 2016; Kagumba and Al-Dahhan, 2015; Youssef et al., 2014), which is attributed by the coarsely distributed local measurement positions. Recently, Al-Al-Mesfer et al. (2016) presented holdup profiles with slight fluctuations when internals are inserted but only results from one cutting line through the cross-sectional images are shown. In contrast, the ultrafast X-ray tomography assesses the local gas holdup at every particular position in the cross-section at spatial resolution down to 1 mm, which otherwise can only be obtained theoretically via CFD simulations as performed by Larachi et al. (2006). They returned a strongly fluctuating liquid velocity profile with several inversion points in the vicinity of the tube walls, which further confirms that the liquid profile is strongly linked with the radial gas holdup profile (Gupta et al., 2001; Ong et al., 2009). As a consequence, it is debatable whether available velocity models (Gupta et al., 2001; Vitankar and Joshi, 2002) are applicable for columns with internals to cope with multiple regions of upflow and downflow (Larachi et al., 2006), respectively. Every inserted tube provides an additional liquid-wall interface with the typical no-slip boundary condition. Accordingly, liquid velocity profiles, and thus, small circulation zones in sub-channels are likely to evolve. On the other hand, larger circulation zones are formed at the wall region, which is kept free of internals.

To further assess the contributions of certain column regions to the total gas holdup, the cross-section has been divided into a core area of the bundle ($0 \leq r/R \leq 0.75$) and a wall region ($0.75 \leq r/R \leq 1.0$). The areas of the two regions occupy approx. 45 % and 55 % of the available cross-section, respectively. For the empty counterpart, they occupy 56.25 % and 43.75 %, respectively.

The division is color-coded in Figure 9. Beyond the analysis of the holdup in these regions, the flow in specific sub-channels from core and wall region of the bundle is characterized below in Section 3.2.2.

Figure 9 allocates the share of the respective cross-sectional regions to the total gas holdup for all configurations at superficial gas velocity of 2 and 20 $cm\,s^{-1}$. The dashed lines indicate the areas of the respective regions, which is rather same for all internals' configurations. Coincidence of the dashed line with the boundaries of the zones would denote uniform gas holdup distribution; any deviation, however, denotes a skewed share. The share of the gas holdup in the empty bubble column follows the known parabolic shape with disproportionately high gas holdup in the center and low gas holdup near the wall. The insertion of the tubes has remarkable effects on the respective share at homogeneous flow conditions ($u_g = 2\,cm\,s^{-1}$). The internals shift the gas holdup towards the wall and invert the profile compared to the empty BCR. This is most remarkable for the configurations with the largest flow resistance (*t8*, *s8*, *su8*). At high gas superficial velocity of 20 $cm\,s^{-1}$ similar trends are observed for the internals, however, the gas holdup is slightly more homogenized.

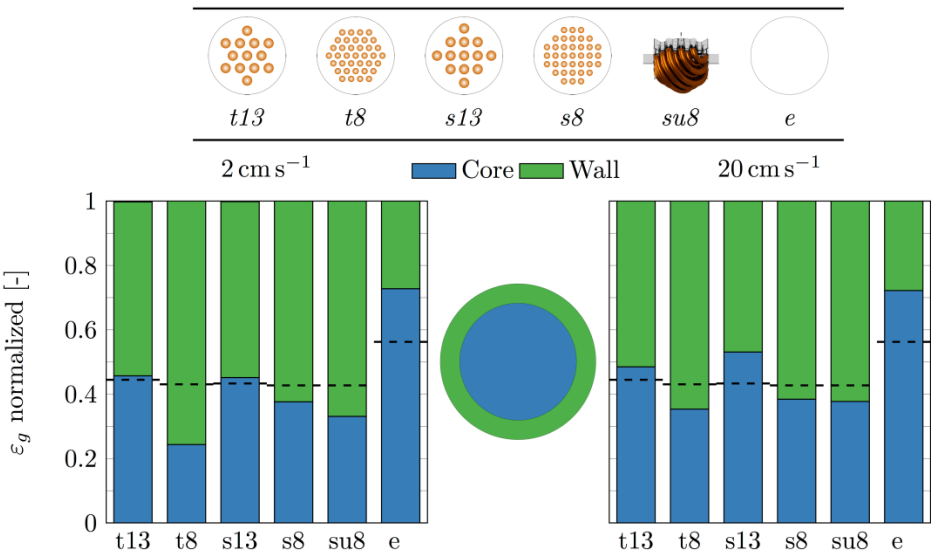

Figure 9: Share of the gas holdup for core and wall region (dashed lines denote the respective area occupied by the respective zones).

To further reveal the effect of the altered share of the respective regions to the total gas holdup, the center line holdup for square 8 internal type (*s8*) and the empty (*e*) counterpart is shown for 2, 6 and 20 cm s^{-1} covering homogeneous and heterogeneous flow regime.

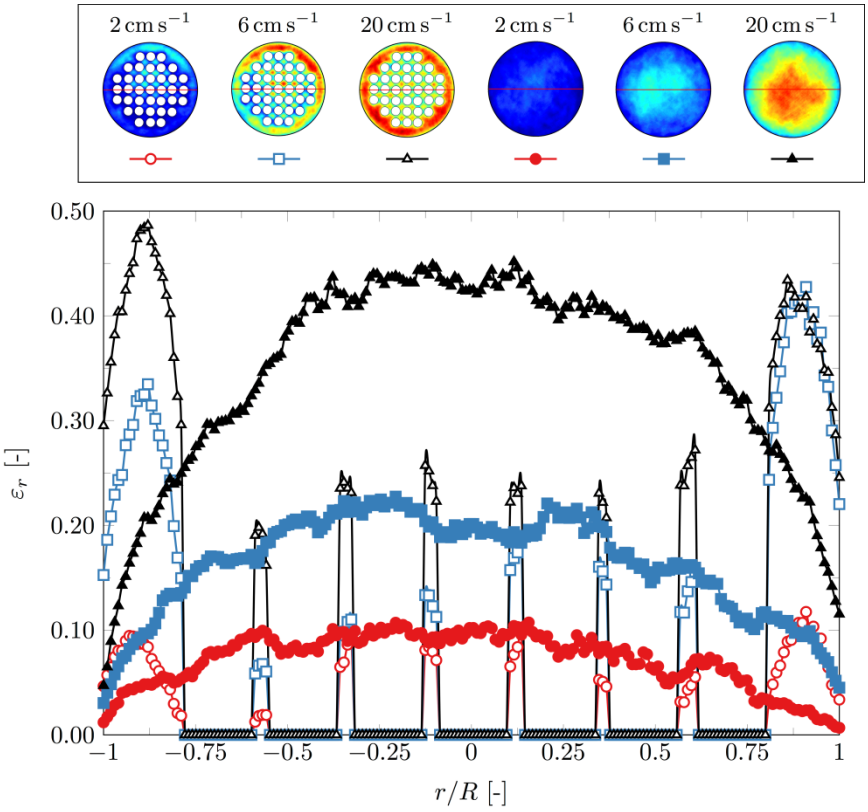

Figure 10: Time-averaged center line holdup profile for an empty (*e*) and square 8 (*s8*) bubble column.

Contrary to the known parabolic profile, which induce the liquid circulation in empty bubble columns (Schweitzer et al., 2001; Thorat et al., 1998; Wu et al., 2001), the gas holdup lowers significantly across the bundle featuring virtually a flat parabolic shape and peaks at the wall zone. Within the sub-channels, parabolic profiles evolve, too.

Considering these characteristic patterns, liquid eddy rotation can be assumed within the bundle. It gets visible from Figure 10 that small and large scale circulation are overlapped, which is shown by the small peaks within the tube bundle and the large peaks at the wall area. This was also

concluded by Forret et al. (2003). The small-scale circulations (eddies), which are driven by the gas holdup profile within the sub-channels (considering core holdup profile), are spinning towards the column wall. Large-scale circulation (considering the whole holdup profile and connecting virtually the holdup peaks) towards the column center result in an airlift-like flow structures contrary to the opposing circulation observed for empty columns. Generally, there is a parabolic holdup profile within the tube bundle visible. However, considering modelling purposes, the reactor cannot be treated as an empty BCR because the wall peaking for the holdup profile is observed. Eventually, it can be concluded that the velocity patterns and anticipated liquid mixing in bubble columns with internals challenge future hydrodynamic modeling approaches, for example, in terms of compartmenting the column in zones with ascending and descending flow for every sub-channel.

3.2 Gas dynamics and bubble properties

Beyond the time-averaged gas holdup analysis, the dynamics of the gas phase were studied in detail. In particular, evolving gas phase morphology, bubble number flux and bubble size distribution are analyzed for the entire column cross-section as well as for sub-channels at various radial positions.

3.2.1 Flow pattern and bubble size distribution

The ultrafast X-ray facility allows disclosing the gas flow structure and morphology within the individual sub-channels of the tube bundles. Basically, every bubble is detected and characterized as explained in Section 2.4.

To assess the influence of internals on the bubble formation - which basically concerns the bubble breakup efficiency - the resulting bubble size distributions (BSD) are exemplarily shown in Figure 11 (binary bubble data can be viewed in the supplementary material). The BSDs are represented as gas holdup carried by a specific bubble class ($\measuredangle\varepsilon/\measuredangle d_e$) for homogeneous bubbly ($u_g = 2\,\mathrm{cm\,s^{-1}}$) and churn-turbulent flow ($u_g = 20\,\mathrm{cm\,s^{-1}}$) (Deckwer, 1992; Nedeltchev et al., 2014)

for all configurations. In addition, pseudo 3D plots of the gas flow morphology, compiled from 1000 consecutive cross-sectional images using ImageJ, are embedded. The tube bundles are only adumbrated for the sake of (visual) clarity and to highlight the gas phase around the bundle. It should be noted that the vertical axis of the embedded gas flow structures features the measurement time.

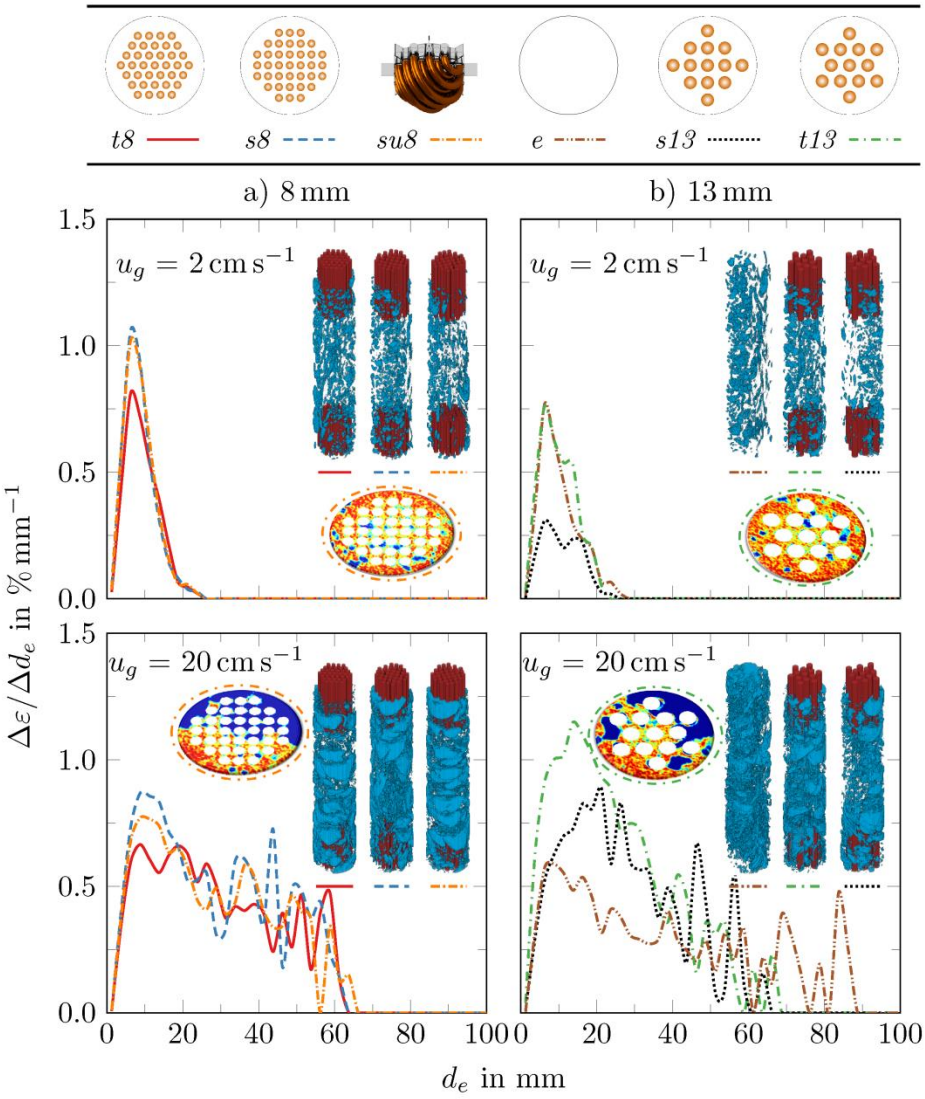

Figure 11: Bubble size distribution with respect to the holdup fraction in a specific bubble class and corresponding pseudo 3D plots of the gas flow morphology.

For the bubbly flow at low superficial gas velocities ($u_g = 2\,cm\,s^{-1}$, upper row), the BSD is narrow, indicating a rather uniform bubble size due to low bubble-bubble and bubbles-internals interactions. The gas bubbles rise nearly undisturbed. At high superficial gas velocity ($u_g = 20\,cm\,s^{-1}$, lower row), coalescence of bubbles widens the bubble size spectra significantly with different impact of the various internals. Largest bubbles are observed for the empty bubble column with equivalent bubble diameters up to 85 mm. At these conditions, such narrow columns operate at the transition between churn-turbulent flow and slug flow with bubbles frequently covering the major part of the cross-section. Contrary, the internals restrict the formation of such large bubbles and the maximum equivalent diameters are approx. 60 mm. A distinct peak can be found for the internals with 8 mm tubes (*s8*, *t8*, *su8*) at approx. 10 mm equivalent bubble diameter, which is attributed to the small hydraulic diameter of 7.6 mm for the square 8 (*s8* and *su8*) configurations and 5.6 mm for the triangular 8 (*t8*) configuration. For the configurations with 13 mm tubes (*s13*, *t13*), the BSDs peak at approx. 20 mm, which corresponds to hydraulic diameters of 11.8 mm (*s13*) and 8.9 mm (*t13*). The difference between the BSD of the configurations (*s13*) and (*t13*) can be explained by sub-channel contour and the hydraulic diameter of the sub-channels. The triangular area and the corresponding hydraulic diameter are clearly smaller. No noticeable impact of the U-tube bottom design (*su8*) configuration was observed.

The pseudo 3D plots in Figure 11 further illustrate the effect of the internals on the flow structure. With tube bundles bubbles preferentially rise in the wall region, which agrees with the observation reported by others (Li and Prakash, 2001; Youssef, 2010). Eventually, this displacing effect by the internals leads to the frequent formation of large connected gas structures at high superficial gas velocities, which are stabilized by the column wall. Such pulsing phenomena are clearly visible in Figure 11. The largest connected gas structures nearly reach the column center and enclose adjacent tubes. With increasing column diameter, however, such wall-stabilized

pulsing is not expected, which is similar to the slug flow regime, which does not exist in empty bubble columns with diameters larger than 0.15 m (Deckwer, 1992).

3.2.2 Sub-channel fraction

In terms of heat transfer performance, the gas-liquid flow and its dynamics in the individual channels within the tube bundle are crucial. Figure 12 shows pseudo 3D plots for a sub-channel in the outer zone of the tube bundle (left subfigure) and in the inner core (right subfigure) as well as the corresponding BSDs at homogeneous (2 cm s^{-1}, upper row) and heterogeneous flow (20 cm s^{-1}, lower row) conditions. At bubbly flow, the bubbles evolve as a bubble train with low interactions (contact) with the surrounding tube walls. At higher superficial gas velocity, Taylor-like bubbles are occupying the entire sub-channel cross-section confined by the surrounding tubes (lower row in Figure 12) similar to Taylor bubbles known from micro and mini channels of various shapes (Haghnegahdar et al., 2016; Triplett et al., 1999; Zhao and Bi, 2001). Such slug flow with elongated bubbles was observed for all internals' configurations at churn-turbulent flow conditions. However, when applying the U-tube bottom design, the elongated bubble formation is somewhat suppressed and a dispersed bubbly flow with comparatively smaller bubbles is established in the sub-channels (not shown here). Furthermore, a lower formation frequency of the gas bubbles was determined. The formation of elongated gas bubbles in the sub-channels has crucial consequences for the heat transfer in bubble columns. It was confirmed that the occurrence of Taylor bubbles within the micro channels is a very effective method to enhance the local heat transfer due to the increased bubble slip, which leads to an enhanced liquid mixing in the liquid slugs (Mehta and Khandekar, 2014). For bubble column reactors with internals, however, Westermeyer-Benz (1992) showed that for internals with denser tubes arrangements, the heat transfer coefficient decreases compared to a looser arrangement. Hence, the formation of elongated bubbles, which is given for densely packed tube bundles, has a slightly negative effect on the heat transfer. Therefore, phenomena from micro or milli channels must not be scaled to bubble column reactors with dense internals.

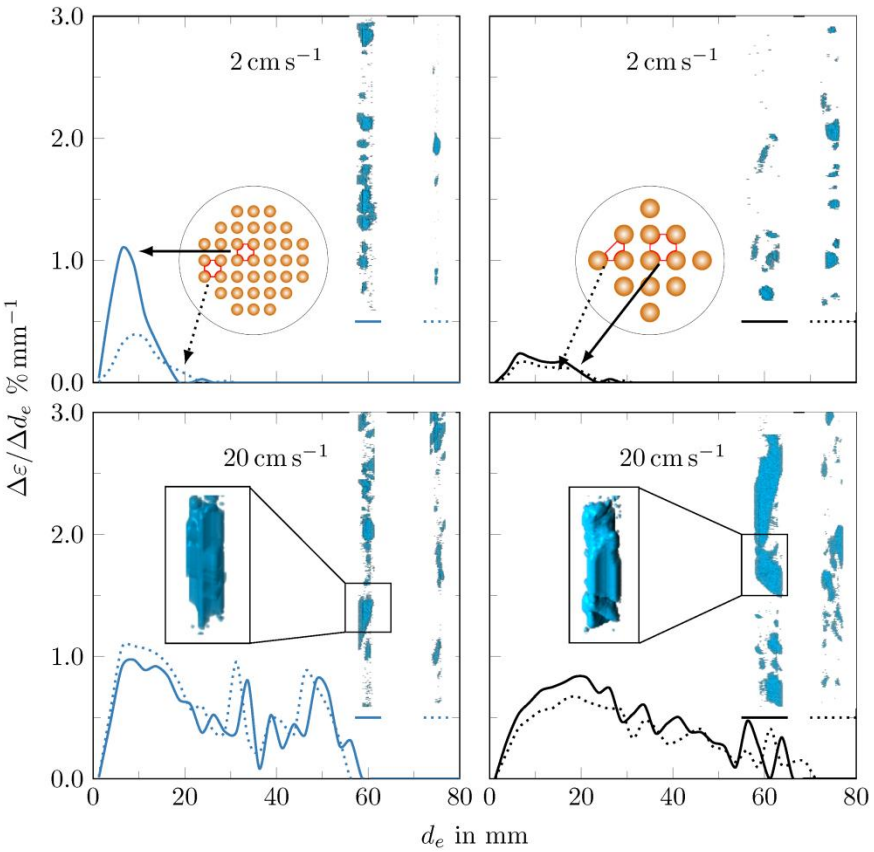

Figure 12: Comparison between inner and outer sub-channel bubble size distribution for square tube bundle configurations *s8* (d_h = 7.6 mm) and (*s13*) (d_h = 11.8 mm).

The corresponding BSDs for the sub-channels of the square configurations (*s13* and *s8*) in Figure 12 reveal that the effect of the sub-channel position within the tube bundle has no remarkable effect. However, at lower superficial gas velocity, a distinct peak can be observed for the dense configuration (*s8*) caused by the narrow sub-channel with a hydraulic diameter of 7.6 mm, while for the larger sub-channel (*s13*), a slightly bimodal distribution is observed with the first peak comparable to *s8* and the second one at about 18 mm coinciding with the hydraulic diameter. At high flow rate, both configurations feature wide BSDs with a slight tendency towards smaller bubbles for the denser internal.

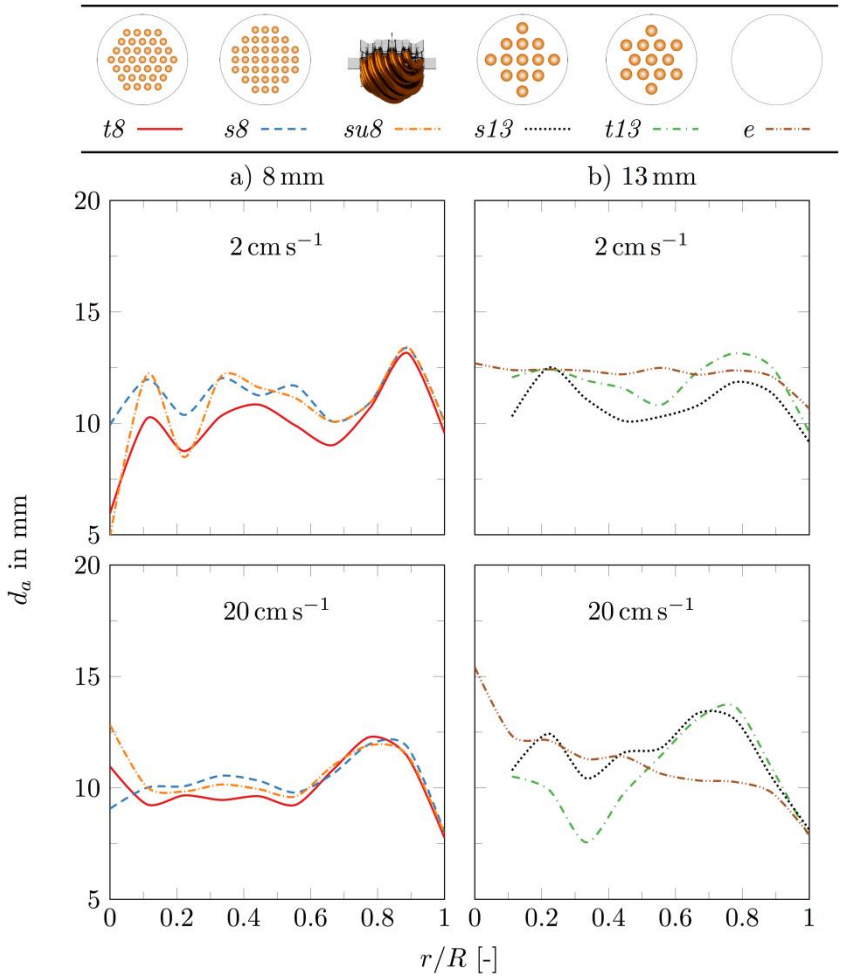

Figure 13: Time-averaged radial bubble size distribution for homogeneous (upper row) and heterogeneous (lower row) flow conditions.

In addition, the time-averaged bubble size for the various internals at homogeneous and heterogeneous flow conditions is shown in Figure 13. For the columns with internals, the average bubble diameter shows a wavy trend similar to the holdup profile, which corresponds to the available free area within the cross-section. However, more large bubbles are formed at the wall region as mentioned above, which is due to the geometrical specifications of the tube bundle. It has to be noted that the average bubble size is smaller for internals within the tube bundle region compared to the empty bubble column. For internals with the smaller tubes, smaller bubbles are formed, which is attributed to the smaller hydraulic diameter of the bundle. For the empty counterpart, the average bubble diameter along the radius remains constant for homogeneous conditions. With increasing superficial gas velocity, large bubbles move towards the center of the

column, confirming the typical parabolic gas holdup profile. With increasing superficial gas velocity the average bubble size increases too, which was already revealed in Figure 11.

Similarly to the gas holdup contribution to different regions of the column cross-section shown in Section 3.1.2 (Figure 9), the respective contributions of the local bubble number flux are summarized in Figure 14. Again, the dashed lines indicate the areas of the respective regions and a coincidence of the dashed line with the boundaries of the zones would denote a uniform bubble appearance in the two zones. Comparing the two areas, it gets clear that most of the bubbles will be formed in the wall region and lesser bubbles will be formed in the core region when internals are inserted with larger tubes (13 mm). However, for smaller tubes (8 mm) and a higher flow resistance, more bubbles are detected in the core of the column. For the empty counterpart, however, most bubbles are formed in the wall region. Keeping in mind that the highest gas holdup is in the center (see Figure 10), it can be concluded that larger bubbles rise in the core region of the empty bubble column. Contrary, for the bubble columns with internals, large bubbles preferably rise in the wall region (see also holdup profile in Figure 8) as they are being stabilized by the column wall and the flow resistance is lesser compared to the flow inside the bundle. In the well-developed churn-turbulent flow regime, the share of the bubble number flux is equally distributed between the two zones, when internals are inserted.

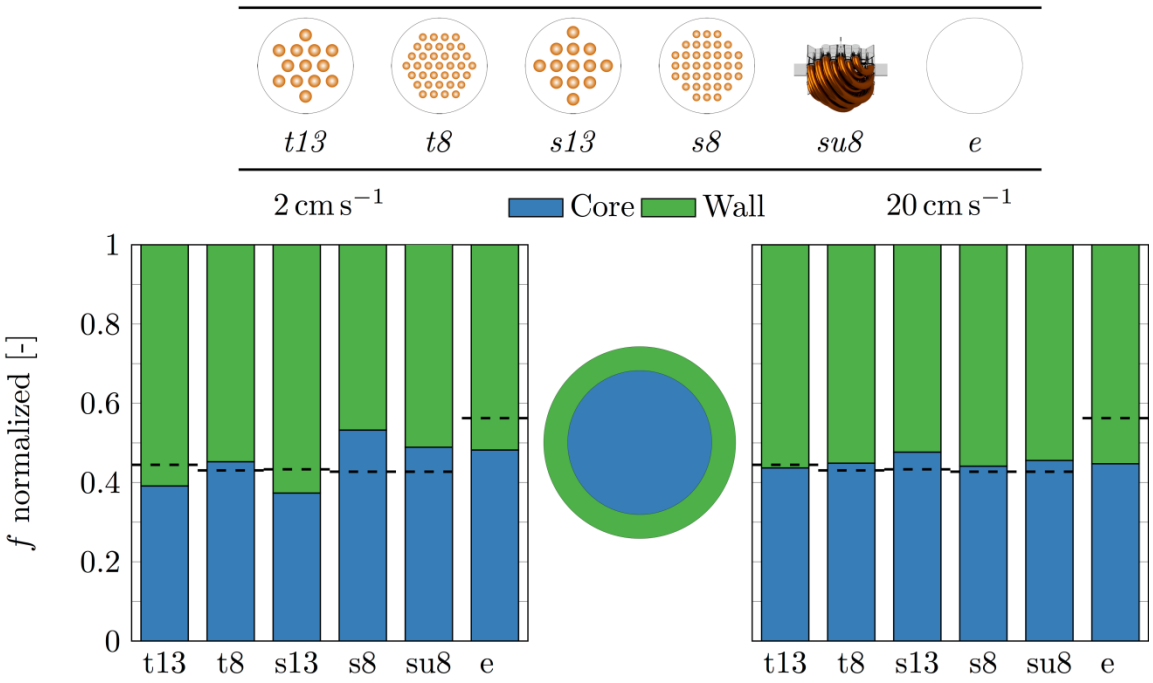

Figure 14: Share of the bubble number flux for core and wall region (dashed lines denote the respective area occupied by the respective zones).

Figure 15 illustrates the positions of the bubbles (bubble centroids) detected during a measurement time of one second within the respective sub-channels.

Two sub-channels were selected representing the flow structure in the most outer (wall sub-channel) and the most inner (center sub-channel) part of the internal, respectively (selected channels are highlighted in Figure 15). There is quite a large deviation between in the number of detected bubbles with clearly lower bubble number flux in the wall sub-channel. Contrary to all other configurations, fewer bubbles pass through the center of the column for the U-tube bottom design, as there bubbles are redirected towards the wall.

The highest bubble number flux was determined for the square 8 (*s8*) configuration. The lowest, in turn, was found for the triangular 8 (*t8*) configuration, which is attributed to the larger flow resistance in the column core. The center of mass (indicated by the crosses) is in the center of the respective sub-channels for all configurations but the square u8 (*su8*) configuration, which denotes a slight shift to the left for the center and to the right for the wall sub-channel. Thus, it

can be concluded the U-tube bottom design induces a kind of lateral bubble movement with a preferred path. Comparing the two 13 mm configurations, more bubbles are accumulated in the triangular 13 (*t13*) than in the square configuration (*s13*).

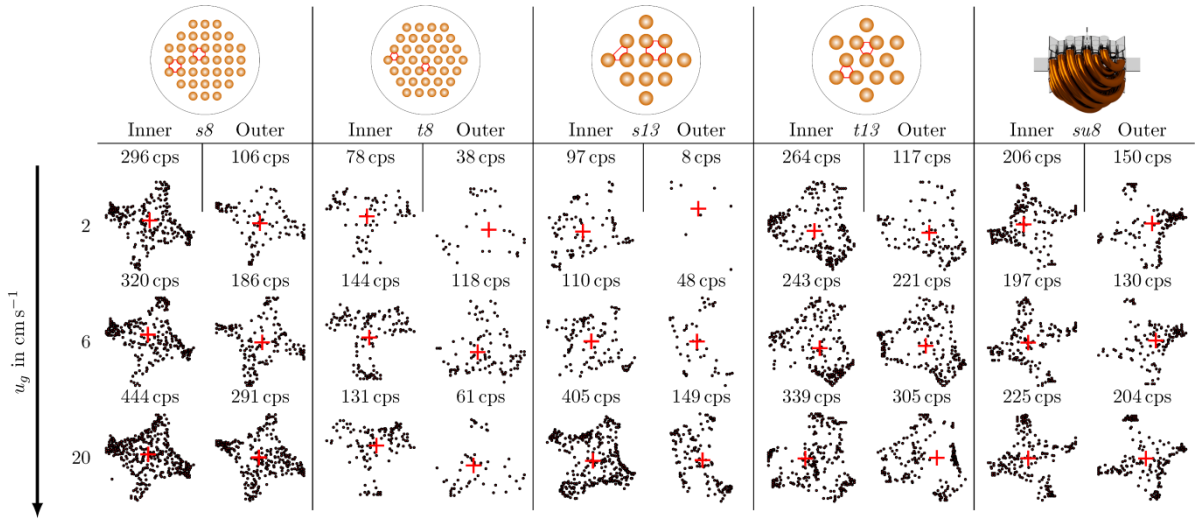

Figure 15: Bubble centroids in center and wall sub-channels of the internals depending on the superficial gas velocity for 1 s.

3.3 Gas holdup correlations

As the total gas holdup for bubble columns with internals has been addressed in previous studies, developed correlations are compared against measurement data from the current article. Comparing local holdup data would be misleading because the profiles obtained in this study are not of a parabolic shape but follow a polynomial trend. Therefore, current models, which were developed for empty bubble columns, are not considered here.

Table 3 summarizes the available holdup correlations, which have been used as they are developed from a comparably large database of column diameters, internal diameters, coverage and geometries valid for a wider range of superficial gas velocities. The correlations by Westermeyer-Benz (1992) and Berg (1993) consider various bubbly flow regime conditions.

Table 3: Gas holdup correlations from literature.

Author	Correlation	Conditions
Yamashita (1987)	$\frac{\varepsilon_{\mathrm{g}}}{1-\varepsilon_{\mathrm{g}}} = 0.03 u_{\mathrm{g}}$	
Westermeyer-Benz (1992)	$\varepsilon_{\mathrm{g}} = S$	$\frac{u_{\mathrm{g,eff}}^3}{\nu_l g}\frac{\rho_{\mathrm{l}}}{\rho_{\mathrm{l}}-\rho_{\mathrm{g}}} \leq 4$ Bubble swarm region
	$\frac{\varepsilon_{\mathrm{g}}}{1-\varepsilon_{\mathrm{g}}} = S$	$\frac{u_{\mathrm{g,eff}}^3}{\nu_l g}\frac{\rho_{\mathrm{l}}}{\rho_{\mathrm{l}}-\rho_{\mathrm{g}}} > 4$ Bubble train region
	$S = C_1(1+C_2 K_{\mathrm{h}})\left(\frac{1}{Fl}\right)^a \left(\frac{u_{\mathrm{g,eff}}^3}{\nu_l g}\frac{\rho_{\mathrm{l}}}{\rho_{\mathrm{l}}-\rho_{\mathrm{g}}}\right)^b$, $C_1 = 0.135, C_2 = 0.5, a = \frac{1}{32}, b = \frac{1}{4}, Fl = \frac{\rho_{\mathrm{l}}\sigma^3}{g\eta_{\mathrm{l}}^4}$	$K_{\mathrm{h}} = 0$ Coalescing $K_{\mathrm{h}} = 1$ Non-coalescing
Berg (1993)	$\varepsilon_{\mathrm{g}} = S$	$\frac{u_{\mathrm{g,eff}}^3}{\nu_l g}\frac{\rho_{\mathrm{l}}}{\rho_{\mathrm{l}}-\rho_{\mathrm{g}}} \leq 1$ Bubble swarm region
	$\varepsilon_{\mathrm{g}} = \frac{S}{1+S}$	$\frac{u_{\mathrm{g,eff}}^3}{\nu_l g}\frac{\rho_{\mathrm{l}}}{\rho_{\mathrm{l}}-\rho_{\mathrm{g}}} > 1$ Bubble train region
	$S = C_1(1+C_2 K_{\mathrm{h}})\left(\frac{u_{\mathrm{g,eff}}^3}{\nu_l g}\frac{\rho_{\mathrm{l}}}{\rho_{\mathrm{l}}-\rho_{\mathrm{g}}}\right)^{aFl^b}$, $C_1 = 0.1$ Bubble swarm region, $C_1 = 0.11$ Bubble train region, $C_2 = 0.93 \quad a = 0.3$, $b = -0.018$	

All correlations are based on the effective superficial gas velocity, which takes the internal-free cross-sectional area into account.

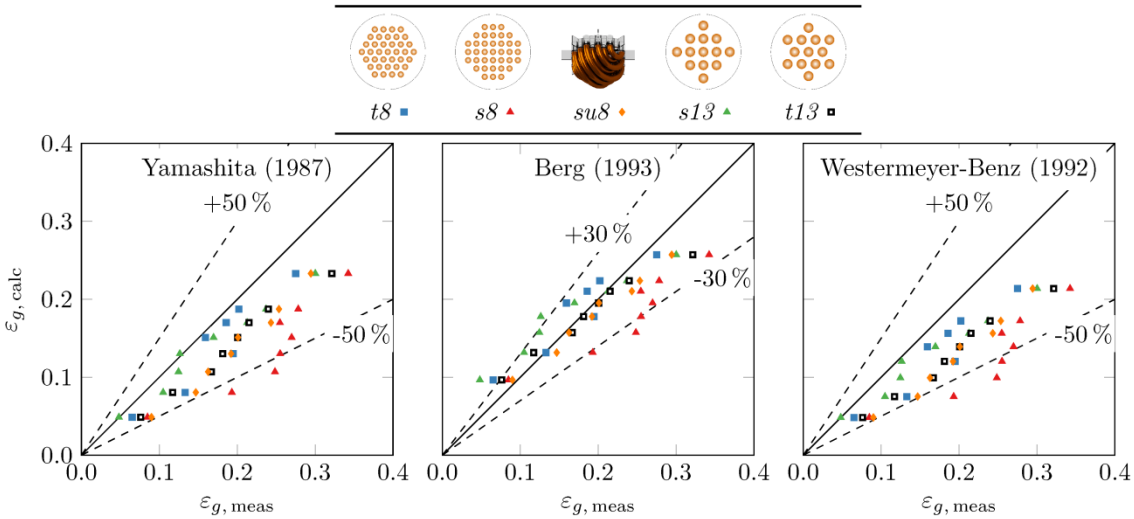

Figure 16: Parity plot of the column total gas holdup comparing measurement data and available correlations (dashed lines represent the deviations provided in the respective subfigures).

Figure 16 shows the parity plots comparing experimental data from this study and predictions using the various correlations summarized in Table 3. Yamashita (1987) and Westermeyer-Benz (1992) consistently under predict the gas holdup. Fair agreement (±30 %) was obtained using the correlation of Berg (1993), which is a slight modification of the correlation proposed by Westermeyer-Benz (1992). This shows that the available correlations do not have a universal character and a better physical description is needed. The overall gas holdup data only from this narrow bubble column are not sufficient to propose a general and advanced correlation. A promising approach for the future is to modify the correlation of Berg (1993) based on dimensionless geometrical factors, which should incorporate tube parameters, such as diameter, coverage, pitch type and size, number of tubes, etc.

4 Conclusions

In this article, the overall hydrodynamics in a bubble column with internals has been studied. In addition, the local parameters in sub-channels of the internal structure were extracted using ultrafast X-ray tomography. Four types of internals were studied with two main patterns, namely, triangular and square pitch, and two tube sizes (8 and 13 mm).

The column total gas holdup is strongly affected by the type of internals used. High flow resistance induced by the internals, e.g. for the smallest tube size and the triangular pitch, redirects the gas bubbles towards the wall region and induces higher rise velocities. Highest holdup in the internals were obtained for the square pitch configuration with 8 mm tube size, where the gas bubbles are trapped within the sub-channel at lower rise velocity leading to higher gas holdup.

The radial gas holdup profiles were found to depend strongly on the installed configuration. Whereas for square configurations, features a non-parabolic profile, triangular patterns provoke a flat profile in the column center. However, for both configurations, the gas holdup near the wall area increases due to the flow resistance in the column center.

For low superficial gas velocities the internals cause higher breakup efficiency. However, at churn-turbulent flow conditions, the influence of the various internals becomes negligible. Regardless of the internals used, elongated gas bubbles evolve within the sub-channels at high superficial gas flow rates.

The square 8 (*s8*) as well as the triangular 13 (*t13*) configuration return highest gas holdup at comparably smallest bubble size distributions, which provides highest interfacial area available for gas-liquid mass transfer, which will be studied soon.

Eventually, all finding hold for narrow bubble columns. Thus, the effect of internals in larger columns will be addressed in a future study.

5 Nomenclature

The authors gratefully acknowledge the European Research Council (ERC StG, No. 307360) for financial support.

6 Nomenclature

Abbreviations

BCR	bubble column reactor
BSD	bubble size distribution
CARPT	computer-automated radioactive particle tracking
CFD	computational fluid dynamics
CT	computed tomography
CSA	cross-sectional area
PDF	probability density function
TEMA	tubular exchanger manufacturers association

Roman symbols

A	column cross-sectional area, m^2
a, b	fitting coefficients, -
A_c	occupied area, %
A_o	free area, %
C_1, C_2	fitting coefficients, -
d	sparger hole diameter, mm
d_a	average bubble diameter, mm
d_o	outer tube diameter, m
d_e	equivalent diameter, mm
D_hyd	hydraulic diameter of whole column, m

d_{hyd}	hydraulic diameter of sub-channel, m
D_{i}	inner column diameter, m
f	bubble number flux, cps
$Fl = \frac{\rho_l \sigma^3}{g \eta_l^4}$	dimensionless fluid number, -
f_{m}	maldistribution factor, -
g	earth acceleration, m s^{-2}
K_{h}	coalescence factor, -
H_z	height of circulation cell, m
l_{V}	voxel edge length, mm
n	number of sparger holes, -
n_{b}	number of bubbles, -
P	pitch, m
px	pixel
r/R	dimensionless radius, -
R	column radius, m
$V_{\mathrm{G,o}}$	inlet gas volumetric flow rate, m^3 s^{-1}
$V_l\ (r)$	liquid velocity profile, m s^{-1}
V_{b}	bubble volume, mm^3
u_{b}	bubble swarm velocity, cm s^{-1}
u_{g}	superficial gas velocity, cm s^{-1}
$u_{\mathrm{g,eff}}$	effective superficial gas velocity, cm s^{-1}
S	holdup coefficient
z/D	dimensionless dinstance from the gas sparger, -

Greek symbols

$\Delta\varepsilon_{\mathrm{g}}/\Delta d_{\mathrm{e}}$	holdup fraction per bubble size class, % mm^{-1}
Δt	time difference, s

Δx	conversion factor, mm pixel^{-1}
ε_g	gas holdup, -
$\varepsilon_{g,corr}$	gas holdup from correlation, -
$\varepsilon_{g,l}$	gas holdup on left side of the column, -
$\varepsilon_{g,meas}$	gas holdup from measurement, -
$\varepsilon_{g,r}$	gas holdup on right side of the column, -
ε_r	radial gas holdup, -
$\boldsymbol{\mu_e}$	empty bubble column reference, -
$\boldsymbol{\mu_f}$	full bubble column reference, -
$\boldsymbol{\mu_n}$	normalized data, -
$\boldsymbol{\mu_r}$	reference data, -
η_l	dynamic liquid viscosity, Pa s
ν_l	kinematic liquid viscosity, m^2 s^{-1}
ρ_i	density of gas or liquid (i = g,l), kg m^{-3}
σ	surface tension, N m^{-1}

7 Bibliography

Al-Mesfer, M.K., Sultan, A.J., Al-Dahhan, M.H., 2016. Impacts of dense heat exchanging internals on gas holdup cross-sectional distributions and profiles of bubble column using gamma ray Computed Tomography (CT) for FT synthesis. Chemical Engineering Journal 300, 317–333.

Azizi, S., Yadav, A., Lau, Y.M., Hampel, U., Roy, S., Schubert, M., 2017. On the experimental investigation of gas-liquid flow in bubble columns using ultrafast X-ray tomography and radioactive particle tracking. Chemical Engineering Science 170, 320–331.

Banowski, M., Beyer, M., Szalinski, L., Lucas, D., Hampel, U., 2017. Comparative study of ultrafast X-ray tomography and wire-mesh sensors for vertical gas–liquid pipe flows. Flow Measurement and Instrumentation 53, Part A, 95–106.

Banowski, M., Lucas, D., Szalinski, L., 2015. A new algorithm for segmentation of ultrafast X-ray tomographed gas-liquid flows. International Journal of Thermal Sciences 90, 311–322.

Barthel, F., Bieberle, M., Hoppe, D., Banowski, M., Hampel, U., 2015. Velocity measurement for two-phase flows based on ultrafast X-ray tomography. Flow Measurement and Instrumentation 46, 196–203.

Berg, S., 1993. Zur Gasgehaltsverteilung und zum Verweilzeitverhalten der Gasphase in Blasensäulen mit längsangeströmten Rohrbündeleinbauten. TU Dortmund.

Berg, S., Schlüter, S., 1995. Rückvermischung in Blasensäulen mit Einbauten. Chemie Ingenieur Technik 67, 289–299.

Berg, S., Steiff, A., Weinspach, P.-M., 1992. Gasphasenvermischung in Blasensäulen mit Einbauten. Chemie Ingenieur Technik 64, 453–456.

Berg, S., Steiff, A., Weinspach, P.-M., 1994. Gasgehaltsverteilung und Verweilzeitverhalten der Gasphase in Blasensäulen mit längsangeströmten Rohrbündeleinbauten. Chemie Ingenieur Technik 66, 724–727.

Bernemann, K., 1989. Zur Fluiddynamik und zum Vermischungsverhalten der flüssigen Phasen in Blasensäulen mit längsangeströmten Rohrbündeln. TU Dortmund.

Bernemann, K., Steiff, A., Weinspach, P.-M., 1991. Zum Einfluß von längsangeströmten Rohrbündeln auf die großräumige Flüssigkeitsströmung in Blasensäulen. Chemie Ingenieur Technik 63, 76–77.

Bieberle, M., Barthel, F., 2016. Combined phase distribution and particle velocity measurement in spout fluidized beds by ultrafast X-ray computed tomography. Chemical Engineering Journal 285, 218–227.

Bieberle, M., Barthel, F., Hoppe, D., Banowski, M., Wagner, M., Lucas, D., Stürzel, T., Hampel, U., 2012. Ultrafast electron beam X-ray computed tomography for 2D and 3D two-phase flow imaging. In: 2012IEEEInternationalConference Imaging SystemsTechniquesProceedings. pp. 605–610.

Bieberle, M., Barthel, F., Menz, H.-J., Mayer, H.-G., Hampel, U., 2011. Ultrafast three-dimensional x-ray computed tomography. Applied Physics Letters 98, 034101.

Bieberle, M., Fischer, F., Schleicher, E., Hampel, U., Koch, D., C. Aktay, K.S. d., Menz, H.-J., Mayer, H.-G., 2007. Ultrafast limited-angle-type x-ray tomography. Applied Physics Letters 91, 123516.

Casanave, D., Galtier, P., Viltard, J.C., 1999. Process and apparatus for operation of a slurry bubble column with application to the fischer-tropsch synthesis.

Chen, J., Li, F., Degaleesan, S., Gupta, P., Al-Dahhan, M.H., Dudukovic, M.P., Toseland, B.A., 1999. Fluid dynamic parameters in bubble columns with internals. Chemical Engineering Science 54, 2187–2197.

De, S.K., Ghosh, S., Parichha, R.K., De, P., 1999. Gas Hold-Up in Two-Phase System with Internals. Indian Chem. Engr. 41.

Deckwer, W.D., 1992. Bubble Column Reactors. John Wiley & Sons Inc.

Deckwer, W.-D., Burckhart, R., Zoll, G., 1974. Mixing and mass transfer in tall bubble columns. Chemical Engineering Science 29, 2177–2188.

Drahoš, J., Zahradnık, J., Puncochár, M., Fialová, M., Bradka, F., 1991. Effect of operating conditions on the characteristics of pressure fluctuations in a bubble column. Chemical Engineering and Processing: Process Intensification 29, 107–115.

Fischer, F., Hoppe, D., Schleicher, E., Mattausch, G., Flaske, H., Bartel, R., Hampel, U., 2008. An ultra fast electron beam x-ray tomography scanner. Measurement Science and Technology 19, (094002) 1–11.

Forret, A., Schweitzer, J.-M., Gauthier, T., Krishna, R., Schweich, D., 2003. Liquid Dispersion in Large Diameter Bubble Columns, with and without Internals. The Canadian Journal of Chemical Engineering 81, 360–366.

George, K.J.H., 2015. Investigations in Hydrodynamics and Mixing Pattern in the Bubble Column Equipped with Internals. The University of Western Ontario.

Guan, X., Gao, Y., Tian, Z., Wang, L., Cheng, Y., Li, X., 2015. Hydrodynamics in bubble columns with pin-fin tube internals. Chemical Engineering Research and Design 102, 196–206.

Guan, X., Li, Z., Wang, L., Cheng, Y., Li, X., 2014. CFD Simulation of Bubble Dynamics in Bubble Columns with Internals. Industrial and Engineering Chemistry Research 53, 16529–16538.

Gupta, P., Ong, B., Al-Dahhan, M.H., Dudukovic, M.P., Toseland, B.A., 2001. Hydrodynamics of churn turbulent bubble columns: gas-liquid recirculation and mechanistic modeling. Catalysis Today 64, 253–269.

Haghnegahdar, M., Boden, S., Hampel, U., 2016. Investigation of mass transfer in milli-channels using high-resolution microfocus X-ray imaging. International Journal of Heat and Mass Transfer 93, 653–664.

Hamed, M., 2012. Hydrodynamics Mixing and Mass Transfer in Bubble Columns with Internals. Washington University St. Louis.

Hawthorne, W.H., Ibsen, M.D., Pedersen, P.S., Bohn, M.S., 2006. Fischer-tropsch slurry reactor cooling tube arrangement.

Hensman, J., 2004. Fischer-tropsch process.

Hugues, F., Szymkowiak, B., Viguie, J.C., Schweitzer, J.M., Munier, M., Chretien, D., Caprani, E., Douziech, D., 2010. Internal exchanger for gas-liquid-solid reactor for fischer-tropsch synthesis.

Jakobsen, H.A., Lindborg, H., Dorao, C.A., 2005. Modeling of Bubble Column Reactors: Progress and Limitations. Industrial & Engineering Chemistry Research 44, 5107–5151.

Jasim, A., 2016. The impact of heat exchanging internals on hydrodynamics of bubble column reactor. Missouri University of Science and Technology.

Jhawar, A.K., 2011. Effects of Internals Configuration on Heat Transfer and Hydrodynamics in Bubble Columns with and witwith solid particles. The University of Western Ontario.

Jhawar, A.K., Prakash, A., 2014. Bubble column with internals: Effects on hydrodynamics and local heat transfer. Chemical Engineering Research and Design 92, 25–33.

Joshi, J.B., Shah, Y.T., 1981. Invited Review Hydrodynamic and Mixing Models for Bubble Column Reactors. Chemical Engineering Communications 11, 165–199.

Kagumba, M.O.O., 2013. Heat transfer and Bubble Dynamics in Bubble and slurry Bubble column with internals for Fischer-Tropsch synthesis of clean alternative fuels and chemicals. Missouri University of Science and technology.

Kagumba, M.O.O., Al-Dahhan, M.H., 2015. Impact of Internals Size and Configuration on Bubble Dynamics in Bubble Columns for Alternative Clean Fuels Production. Industrial & Engineering Chemistry Research 54, 1359–1372.

Kalaga, D.V., Yadav, A., Goswami, S., Bhusare, V., Pant, H.J., Dalvi, S.V., Joshi, J.B., Roy, S., 2017. Comparative analysis of liquid hydrodynamics in a co-current flow-through bubble column with densely packed internals via radiotracing and Radioactive Particle Tracking (RPT). Chemical Engineering Science.

Kölbel, H., Ackermann, P., 1958. Apparatus for carrying out gaseous catalytic reactions in liquid medium.

Korte, H.-J., 1987. Wärmeübergang in Blasensäulen mit und ohne Einbauten. TU Dortmund.

Laborde-Boutet, C., Larachi, F., Dromard, N., Delsart, O., Béliard, P.-E., Schweich, D., 2010. CFD simulations of hydrodynamic/thermal coupling phenomena in a bubble column with internals. AIChE Journal 56, 2397–2411.

Larachi, F., Desvigne, D., Donnat, L., Schweich, D., 2006. Simulating the effects of liquid circulation in bubble columns with internals. Chemical Engineering Science 61, 4195–4206.

Lau, Y.M., Müller, K., Azizi, S., Schubert, M., 2016. Voronoï analysis of bubbly flows via ultrafast X-ray tomographic imaging. Experiments in Fluids 57, (57:35) 1–12.

Lee, H.T., Jung, H., Chun, D.H., Kim, H.J., Yang, J.I., Yang, J.H., 2009. A cooling system for elimination of heat of reaction at fischer-tropsch slurry bubble column reactor.

Li, H., Prakash, A., 2001. Survey of heat transfer mechanisms in a slurry bubble column. The Canadian Journal of Chemical Engineering 79, 717–725.

Luo, H., Svendsen, H.F., 1991. Turbulent circulation in bubble columns from eddy viscosity distributions of single-phase pipe flow. The Canadian Journal of Chemical Engineering 69, 1389–1394.

Maretto, C., Piccolo, V., 1998. Fischer-Tropsch process with a multistage bubble column reactor.

Maretto, C., Piccolo, V., Viguie, J.C., Ferschneider, G., 2002. Fischer-Tropsch process.

Mehta, B., Khandekar, S., 2014. Taylor bubble-train flows and heat transfer in the context of Pulsating Heat Pipes. International Journal of Heat and Mass Transfer 79, 279–290.

Möller, F., Seiler, T., Lau, Y.M., Weber, M., Weber, M., Hampel, U., Schubert, M., 2017. Performance comparison between different sparger plate orifice patterns: Hydrodynamic investigation using ultrafast X-ray tomography. Chemical Engineering Journal 316, 857–871.

Ong, B.C., Gupta, P., Youssef, A., Al-Dahhan, M., Duduković, M.P., 2009. Computed Tomographic Investigation of the Influence of Gas Sparger Design on Gas Holdup Distribution in a Bubble Column. Industrial & Engineering Chemistry Research 48, 58–68.

Piccolo, V., Bonomi, S., Piazza, M., 2012. Modular reactor for exothermic/endothermic chemical reactions.

Pradhan, A.K., Parichha, R.K., De, P., 1993. Gas hold-up in non-newtonian solutions in a bubble column with internals. The Canadian Journal of Chemical Engineering 71, 468–471.

Prince, M.J., Blanch, H.W., 1990. Bubble coalescence and break-up in air-sparged bubble columns. AIChE Journal 36, 1485–1499.

Schlüter, S., Steiff, A., Weinspach, P.-M., 1995. Heat transfer in two- and three-phase bubble column reactors with internals. Chemical Engineering and Processing: Process Intensification 34, 157–172.

Schweitzer, J.-M., Bayle, J., Gauthier, T., 2001. Local gas hold-up measurements in fluidized bed and slurry bubble column. Chemical Engineering Science 56, 1103–1110.

Shah, R.K., Sekulic, D.P., 2003. Fundamentals of Heat Exchanger Design. John Wiley & Sons.

Shah, Y.T., Kelkar, B.G., Godbole, S.P., Deckwer, W.-D., 1982. Design parameters estimations for bubble column reactors. AIChE Journal 28, 353–379.

Sharaf, S., Zednikova, M., Ruzicka, M.C., Azzopardi, B.J., 2016. Global and local hydrodynamics of bubble columns - Effect of gas distributor. Chemical Engineering Journal 288, 489–504.

Sie, S.T., Krishna, R., 1999. Fundamentals and selection of advanced Fischer–Tropsch reactors. Applied Catalysis A: General 186, 55–70.

Thorat, B.N., Shevade, A.V., Bhilegaonkar, K.N., Aglawe, R.H., Veera, U.P., Thakre, S.S., Pandit, A.B., Sawant, S.B., Joshi, J.B., 1998. Effect of Sparger Design and Height to Diameter Ratio on Fractional Gas Hold-up in Bubble Columns. Chemical Engineering Research and Design 76, 823–834.

Thulukkanam, K., 2013. Heat Exchanger Design Handbook, 2nd Edition. ed. CRC Press.

Triplett, K.A., Ghiaasiaan, S.M., Abdel-Khalik, S.I., Sadowski, D.L., 1999. Gas–liquid two-phase flow in microchannels Part I: two-phase flow patterns. International Journal of Multiphase Flow 25, 377–394.

Urseanu, M.I., 2000. Scaling up bubble column reactors. Van 't Hoff Institute for Molecular Sciences (HIMS).

Vitankar, V.S., Joshi, J.B., 2002. A Comprehensive One-Dimensional Model for Prediction of Flow Pattern in Bubble Columns. Chemical Engineering Research and Design 80, 499–512.

Wagner, M., Barthel, F., Zalucky, J., Bieberle, M., Hampel, U., 2015. Scatter analysis and correction for ultrafast X-ray tomography. Philosophical Transactions of the Royal Society of London A: Mathematical, Physical and Engineering Sciences 373.

Westermeyer-Benz, H., 1992. Wärmeübergang und Gasgehalt in zwei-und dreiphasig betriebenen Blasensäulenreaktoren mit längseingebauten Rohren. TU Dortmund.

Wilkinson, P.M., Spek, A.P., Dierendonck, L.L. van, 1992. Design parameters estimation for scale-up of high-pressure bubble columns. AIChE Journal 38, 544–554.

Wu, Y., Ong, B.C., Al-Dahhan, M.H., 2001. Predictions of radial gas holdup profiles in bubble column reactors. Chemical Engineering Science 56, 1207–1210.

Yamashita, F., 1987. Effects Of Vertical Pipe And Rod Internals On Gas Holdup In Bubble Columns. Journal of Chemical Engineering of Japan 20, 204–206.

Youssef, A.A., 2010. Fluid Dynamics and Scalue-Up of Bubble Columns with Internals. Washington University St. Louis.

Youssef, A.A., Al-Dahhan, M.H., 2009. Impact of Internals on the Gas Holdup and Bubble Properties of a Bubble Column. Industrial and Engineering Chemistry Research 48, 8007–8013.

Youssef, A.A., Al-Dahhan, M.H., Duduković, M.P., 2013. Bubble Columns with Internals: A Review. International Journal of Chemical Reactor Engineering 11, 169.

Youssef, A.A., Hamed, M.E., Al-Dahhan, M.H., Duduković, M.P., 2014. A new approach for scale-up of bubble column reactors. Chemical Engineering Research and Design 92, 1637–1646.

Zehner, P., 1988. Modellbildung für Mehrphasenströmungen in Reaktoren. Chemie Ingenieur Technik 60, 531–539.

Zhao, T.S., Bi, Q.C., 2001. Co-current air–water two-phase flow patterns in vertical triangular microchannels. International Journal of Multiphase Flow 27, 765–782.